Int. J. Fuzzy Syst. (2021) 23(4):918–936
https://doi.org/10.1007/s40815-020-01030-5

Image Edge Detection: A New Approach Based on Fuzzy Entropy and Fuzzy Divergence

Mario Versaci[1] · **Francesco Carlo Morabito**[1]

Received: 14 January 2020 / Revised: 3 November 2020 / Accepted: 30 November 2020 / Published online: 6 February 2021

Abstract In image pre-processing, edge detection is a non-trivial task. Sometimes, images are affected by vagueness so that the edges of objects are difficult to distinguish. Hence, the usual edge-detecting operators can give unreliable results, thus necessitating the use of fuzzy procedures. In literature, Chaira and Ray approach is a popular technique for fuzzy edge detection in which fuzzy divergence formulation is exploited. However, this approach does not specify the threshold technique must be applied. Then, in this work, starting from Chairy and Ray procedure, we present a new fuzzy edge detector based on both fuzzy divergence (thought and proved to be a distance) and fuzzy entropy minimization for the thresholding sub-step in gray-scale images. Eddy currents, thermal infrared, and electrospinning images were used to test the proposed procedure after their fuzzification by a suitable adaptive S-shaped fuzzy membership function. Moreover, the fuzziness content of each image has been quantified by new specific indices proposed here and formulated in terms of fuzzy divergence. The results have been evaluated by suitable assessment metrics here formulated and are considered to be encouraging when qualitatively and quantitatively compared with those obtained by some well-known I- and II-order edge detectors.

Keywords Image pre-processing · Edge detectors · Fuzzy divergence and entropy

✉ Mario Versaci
mario.versaci@unirc.it

Francesco Carlo Morabito
morabito@unirc.it

[1] DICEAM Department, Cittadella Universitaria, Via Graziella Feo di Vito, 89122 Reggio Calabria, Italy

1 Introduction

Segmentation in image processing (IP) divides a digital image into disjoint regions with homogeneous characteristics with respect to features, resulting in different regions having different characteristics [1–3]. Methodologies use techniques of thresholding [1], grouping [4], compression [5, 6], variational procedures [7], graph partitions [8], Partial Differential Equations (PDEs) and multi-scale approaches [9, 10], and many others [11–15]. Because they have high computational costs, such techniques are undesirable. However, many engineering applications require only the edge detection procedure (which, by the way, could represent the first step of segmentation and registration procedures). Therefore, one needs to use edge-detecting operators to highlight discontinuities in features [1, 11, 16], thereby simplifying the analysis of an image by reducing the data to be processed [17, 18]. Although edge detection is a technique widely addressed in scientific literature, it still arouses great interest due to the numerous fields of application [19–23]. There are many approaches for edge detection (ED). For example, it can be implemented by a search-based method, in which the edge strength is computed by the I-order derivative, after which the local maxima are sought (the Roberts, Prewitt, and Sobel approaches [11, 24–27]). Other ED procedures use the II-order derivative or Laplacian of Gaussian (LoG) or the difference of Gaussian [1, 11, 14, 17, 18]. The LoG produces continuous closed boundaries because it is the zero set of an implicit function; however, it is noise sensitive since it is a II-derivative operator [1, 11, 17, 18]. Moreover, it can produce double edges and undesirable effects due to incomplete segmentation [17, 18, 24]. Then, the LoG extracts the edges by zero-crossing using very time-consuming procedures [1, 11, 16]. Thus, the idea of

using entropy for edge detection has matured and resulted in procedures with lower computational costs [1, 11]. Historically, Albuquerque et al. [28] introduced the maximum entropy principle by using the Tsallis non-extensive entropy, while Sahoo and Arona [29] used 2*D* Renyi entropy, which was obtained from the 2*D* histogram established by the gray value of the pixels and their local average. Since then, scientific works on ED by entropy have been developed exponentially. In particular, multi-threshold values for ED have been computed by using Charvat's and Shannon entropies as well as sophisticated ED techniques that are based on entropy combined with particle swarm optimization algorithms. However, sometimes, edges are not clearly defined; thus, usual approaches can fail. In such cases, Fuzzy Logic (FL) can be used to handle vagueness, ambiguity, or both in an image by introducing suitable Membership Functions (MFs, which are better if made adaptively). This approach makes some Fuzzy Templates (FTs) [17, 18] or fuzzy reasoning reliable fuzzy edge detectors. Fuzzy Sobel ED [17, 18], for example, calculates the gradient by combining special gradients computed in two directions, and edges are detected by thresholding using a trial and error method. If pixels have large differences in gray levels compared with their neighborhood region, then they are classified in a fuzzy edge region; otherwise, they are classified in a fuzzy smooth region. Then, the boundaries of the two regions are determined from four threshold values derived from a difference histogram calculated by the maximum difference in the gray level of each pixel in all eight directions. As performed by Kenneth [30], FTs (denoting the possible edge directions of the image) are convoluted with the image, and the fuzzy similarity between each pixel of the image and the pixel value of each template is evaluated to highlight an edge in the image by combining the obtained similarity values. As a result, the edges are highlighted by alpha-cut threshold operations [17, 18, 30]. Finally, Chaira and Ray [17, 18], starting from the fuzzy Sobel procedure, proposed an ED procedure based on 16 FTs so that the distances between the pixels of the templates and the image are formulated by Fuzzy Divergence (FD), which transforms the image into a matrix of divergences to be properly thresholded. However, although Chaira and Ray procedure the most popular approach for Fuzzy EDs (FEDs) based on FTs, it does not take into account that entropy represents uncertainty. The, in this work we exploit the Fuzzy Entropy (FE) concept in order to describe the information of its uncertainty. It calculates the certainty or uncertainty value of a dataset and helps in choosing the dataset that satisfies the requirement of edge pixels, thus realizing effective edge detection. Therefore, a reliable dataset and reliable ED can be obtained as output with the function. So, in this paper, starting from Chaira and Ray's procedure [17, 18], a new FED approach is presented, as depicted in Fig. 1.

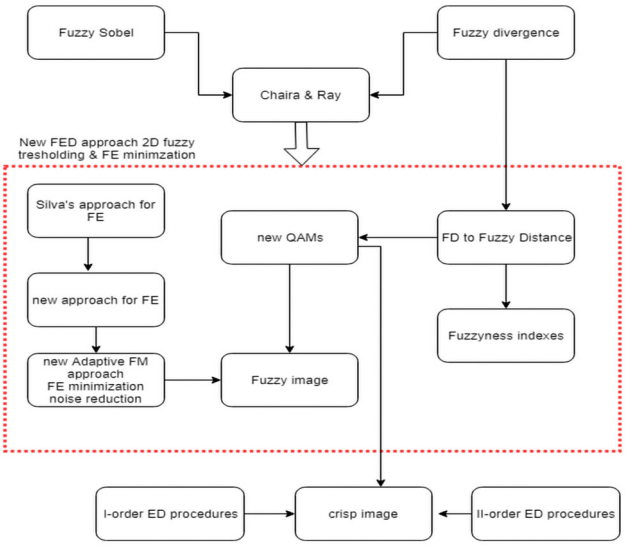

Fig. 1 Flowchart of the proposed FED procedure

The core of the proposed approach (highlighted in red in the flow-chart) is a new FE formulation. In particular, starting from [31] in which a two-dimensional sample entropy was exploited for assessing image texture through irregularity, the new FE approach uses FD as the distances between fuzzified images to take into account the extent of the distance between the first image and the second one and vice versa. In addition, we prove that FD represents a distance between images in a suitable functional space. Moreover, to fuzzify each image, S-shaped membership function has been built by exploiting both FE minimization and noise reduction. Then, to evaluate the fuzziness content of each image, four indexes of fuzziness (IoFs) based on FD computation have been constructed and tested on each image. The results are interesting when quantitatively compared with other well-established ED I- and II-order techniques [1, 2, 17, 18] by using new formulations of reference Quality Assessment Metrics (QAMs) here presented in which the distances among images are computed by means of FD formulation. Furthermore, two nonreference Quality Assessment Metrics (QAMs) [32–34] well-known in literature have bee exploited to confirm the results obtained with the metrics formulated in terms of FD. The paper is structured as follows. After some fuzzy definitions (Sect. 2), the Chaira and Ray approach is presented in Sect. 3. Then, the proposed algorithm as a variant of the Chaira and Ray procedure is presented in Sects. 4, 5 and 6. The procedure, implemented on an Intel Core 2 CPU 1.45 GHz machine and and MatLab® R2017a, was tested on different kind of images (Eddy Currents (ECs) maps [35], Infrared (IR) images [36], and Electrospinning (ES)

Table 1 Acronyms

Acronym	Description	Acronym	Description
IP	Image processing	ED	Edge detection
LoG	Laplacian of Gaussian	FL	Fuzzy logic
FT	Fuzzy template	FE	Fuzzy entropy
FED	Fuzzy edge detection	FD	Fuzzy divergence
MF	Membership function	ECs	Eddy currents
IR	Infrared image	ES	Electrospinning
IoF	Index of fuzziness	QAM	Quality assessment metric
HNF	Homogeneous nanofibers	MSE	Mean square error
MAE	Mean absolute error	SSIM	Structural similarity measure
GSSIM	Gradient SSIM		

maps [37] described in Sect. 7). A brief overview on first/second-order edge detection procedures is presented in Sects. 8 and 9, respectively. Four Indexes of Fuzziness (IoFs) were made to verify the fuzziness content in each image as detailed in Sect. 10. The results are discussed in Sect. 12 and compared, using the new formulation of the reference QAMs formulation and non reference QAMs well-known in literature (Sect. 11), with the results obtained by I- and II-order techniques. Then, some conclusions and perspective are drawn (Sects. 13 and 14). Finally, an appendix details the proof of the Theorem 1. To improve the readability of the paper, the list of acronyms used is shown in Table 1.

2 Basic FL Concepts and Definitions

A 2*D* gray-level image with can be considered as a matrix $\mathbf{I}$ constituted by M rows and N columns with $M \times N$ elements (i, j), $i = 1, \ldots, M$, $j = 1, \ldots, N$ which represent the pixels of $\mathbf{I}$. We associate each pixel (i, j) with its corresponding gray level, a_{ij}, to represent its brightness on the range [0, 255].

Let us consider $\mathbf{I}_{norm}$ to be a new image in which each pixel has a related gray level $\hat{a_{ij}} = (a_{ij}/255) \in [0, 1]$. On $\mathbf{I}_{norm}$, a fuzzy MF, defined as $m_{\mathbf{I}_{\text{norm}}}(\hat{a_{ij}}) : \mathbf{I}_{\text{norm}} \rightarrow [0, 1]$, formalizes the extent to which $\hat{a_{ij}}$ belongs to $\mathbf{I}_{\text{norm}}$. If $m_{\mathbf{I}_{\text{norm}}}(\hat{a_{ij}}) = 1$, then $\hat{a_{ij}}$ belongs to $\mathbf{I}_{\text{norm}}$ in its entirety; if $m_{\mathbf{I}_{\text{norm}}}(\hat{a_{ij}}) = 0$, then $\hat{a_{ij}}$ does not belong to $\mathbf{I}_{\text{norm}}$ at all; finally, if $m_{\mathbf{I}_{\text{norm}}}(\hat{a_{ij}}) \in (0, 1)$, then $\hat{a_{ij}}$ partially belongs to $\mathbf{I}_{\text{norm}}$. Let us consider $F(\mathbf{I}_{\text{norm}})$ as the fuzzified image of $\mathbf{I}_{\text{norm}}$ whose pixels represent $m_{\mathbf{I}}(\hat{a_{ij}})$, $i = 1, \ldots, M$ and $j = 1, \ldots, N$.

Since the proposed procedure is a variant of the Chaira and Ray fuzzy approach, we introduce the FED that they proposed [17, 18].

3 FED: The Chaira and Ray Approach

Chaira and Ray's approach uses the concept of fuzzy divergence to compute the dissimilarity between fuzzified images.

Definition 1 (*Fuzzy divergence*) If U is the universe of discourse, let us consider $FS(U)$ as the set of all fuzzified images on U. The mapping $D : FS(U) \times FS(U) \rightarrow [0, 1]$ is a measure of FD if for each fuzzified images A and B the following conditions are satisfied:

(1) $D(A, B) = D(B, A)$;
(2) $D(A, A) = 0$;
(3) $D(A \cap C, B \cap C) \leq D(A, B)$, $\forall C \in FS(U)$;
(4) $D(A \cup C, B \cup C) \leq D(A, B)$ $\forall C \in FS(U)$.

From the axioms (2) and (4) we easily deduce the non-negativity of the FD measurement.

Chaira and Ray used FD between $\mathbf{I}_{\text{norm}}$ and each of a set of sixteen 3×3 fuzzy templates (FTs), with gray levels $\in \{0.3,\ 0.8\}$, to represent the edge profiles (for details, see [17, 18]). The center of each FT is placed at each pixel position (i, j) over $\mathbf{I}_{\text{norm}}$. With the window of the same size as that of the FT, indicated by $(\mathbf{I}_{norm})_w$, FD was defined as [17, 18]

$$\max_{\text{numberofFTs}} \left[\min_{3\times 3=9} \left(Divergence((\mathbf{I}_{norm})_w, \text{FT}) \right) \right]. \tag{1}$$

In (1), *Divergence* between $(\mathbf{I}_{norm})_w$ and FT is calculated by computing the FD between each of the elements $(\mathbf{I}_{norm})_w(\hat{a_{ij}})$ and FT(i, j) of $(\mathbf{I}_{norm})_w$, respectively. We observe that, fuzzily, to define the total divergence between $(\mathbf{I}_{norm})_w$ and FT, we need to take into account how much $(\mathbf{I}_{norm})_w$ diverges from FT, i.e. $\overline{D}((\mathbf{I}_{norm})_w, \text{FT})$, and, vice versa, how much FT diverges form $(\mathbf{I}_{norm})_w$, i.e. $\overline{D}(\text{FT}, (\mathbf{I}_{\text{norm}})_{\text{w}})$. Then, the total divergence, labeled by $D((\mathbf{I}_{norm})_w, \text{FT})$, can be computed as [17, 18, 35]

$$D((\mathbf{I}_{norm})_w, \mathrm{FT}) = \overline{D}((\mathbf{I}_{norm})_w, \mathrm{FT}) + \overline{\mathrm{D}}(\mathrm{FT}, (\mathbf{I}_{\mathrm{norm}})_{\mathrm{w}}), \tag{2}$$

where

$$\begin{aligned}\overline{D}((\mathbf{I}_{norm})_w, \mathrm{FT}) = \sum_{i=1}^{M}\sum_{j=0}^{N}\Big(1 - \Big(1 - m_{(\mathbf{I}_{norm})_w(\hat{a_{ij}})}\Big) \\ \times\, \mathrm{e}^{\mathrm{m}_{(\mathbf{I}_{\mathrm{norm}})_{\mathrm{w}}(\hat{\mathrm{a}_{\mathrm{ij}}})} - \mathrm{m}_{\mathrm{FT(i,j)}}} - \mathrm{m}_{(\mathbf{I}_{\mathrm{norm}})_{\mathrm{w}}(\hat{\mathrm{a}_{\mathrm{ij}}})} \\ \times\, \mathrm{e}^{\mathrm{m}_{\mathrm{FT(i,j)}} - \mathrm{m}_{(\mathbf{I}_{\mathrm{norm}})_{\mathrm{w}}(\hat{\mathrm{a}_{\mathrm{ij}}})}}\Big)\end{aligned} \tag{3}$$

and

$$\begin{aligned}\overline{D}(\mathrm{FT}, (\mathbf{I}_{\mathrm{norm}})_{\mathrm{w}}) = \sum_{i=1}^{M}\sum_{j=1}^{N}\Big(1 - \Big(1 - m_{\mathrm{FT(i,j)}}\Big) \\ \times\, \mathrm{e}^{\mathrm{m}_{\mathrm{FT(i,j)}} - \mathrm{m}_{(\mathbf{I}_{\mathrm{norm}})_{\mathrm{w}}(\hat{\mathrm{a}_{\mathrm{ij}}})}} - \mathrm{m}_{\mathrm{FT(i,j)}} \\ \times\, \mathrm{e}^{\mathrm{m}_{(\mathbf{I}_{\mathrm{norm}})_{\mathrm{w}}(\hat{\mathrm{a}_{\mathrm{ij}}})} - \mathrm{m}_{\mathrm{FT(i,j)}}}\Big).\end{aligned} \tag{4}$$

Remark 1 We observe that $D((\mathbf{I}_{norm})_w, \mathrm{FT})$, as computed in (2) by (3) and (4), satisfies the four axioms defining a measure of FD [17, 18].

Applying (2), (3), and (4) forms an FD matrix, requiring the use of a threshold procedure to obtain the edge-detected image. Chaira and Ray did not specify which threshold technique must be applied; thus, the choice of threshold procedure for the FD image is left to the sensitivity of the operator. Therefore, in this work, we present a new procedure based on FE in order to take into account the measure of a quantity of fuzzy information gained from a fuzzy construct.

4 The Proposed Algorithm as a Variant of the Chaira and Ray Approach

We premise the following definition.

Definition 2 (Fuzzy Entropy) Let FE be a map defined as $\mathrm{FE} : \mathrm{F}(2^{\mathrm{X}}) \rightarrow [0, 1]$, with X is a generic set. FE, which is a fuzzy set defined on fuzzy sets, is a FE measure if only if satisfies the following three axioms [17]:

(1) $\mathrm{FE(A)} = 0$, if only if $A \in 2^X$ (A nonfuzzy);
(2) $\mathrm{FE(A)} = 1$ if only if $m_A(x_i) = 0.5$, $\forall i$;
(3) $\mathrm{FE(A)} \leq \mathrm{FE(B)}$ if $m_A(x) \leq m_b(x)$ when $m_B(x) \leq 0.5$ and $m_A(x) \geq m_B(x)$ when $m_B(x) > 0.5$;
(4) $\mathrm{FE(A)} = \mathrm{FE(A^c)}$.

Here, as discussed in the previous section, the proposed approach applies the concept of FD between images, as computed in (2), (3), and (4), and the steps of the algorithm substantially overlap with the Chaira and Ray procedure. However, a procedure to threshold the FD matrix using a new approach based on both FE and FD computations (see Sect. 5) is presented.

4.1 The Main Steps of the Proposed Procedure

The FED procedure proposed by the authors in this paper can be divided into the following seven basic steps.

STEP 1. Apply an FT over $\mathbf{I}_{norm}$ by placing the center of FT at each (i, j).
STEP 2. Calculate the FD value between each of the elements of $(\mathbf{I}_{norm})_w$ and the FT, and select the minimum value.
STEP 3. Repeat steps 1-2 for all 16 FTs.
STEP 4. Choose the maximum value among all 16 minimum FD values.
STEP 5. Place the maximum value at the point at which the FT is centered over the image.
STEP 6. Repeat steps 2-5 for all the pixel positions to construct a new divergence matrix.
STEP 7. Threshold the FD matrix by the joint use of FE and FD. Here, the authors propose a new entropic $2D$ fuzzy thresholding method based on minimization of FE and FD, too (see Sect. 5).

Once the FD matrix is computed, for each threshold $T \in [0\ 1]$, a σ-square matrix, $\mathbf{A}^{\sigma}_{\bar{\mathbf{i}},\bar{\mathbf{j}}}(\mathbf{T})$, located on $(\bar{i}, \bar{j})$, is set and considered to be another σ-square window, $\mathbf{A}^{\sigma}_{\mathbf{h},\mathbf{k}}(\mathbf{T})$, located on another pixel (h, k). Their distance, $D^{\sigma}_{\bar{i},\bar{j},h,k}$, is first calculated by FD, $D(\mathbf{A}^{\sigma}_{\bar{\mathbf{i}},\bar{\mathbf{j}}}(\mathbf{T}), \mathbf{A}^{\sigma}_{\mathbf{h},\mathbf{k}}(\mathbf{T}))$. The average value of all FDs obtained by moving (h, k) in all possible positions is then calculated. Moreover, we calculate the further average value obtained by moving $(\bar{i}, \bar{j})$ in all possible positions (indicated by $\chi^{\sigma}(T)$). We repeat the procedure for $\sigma + 1$-square windows and obtain $\chi^{\sigma+1}(T)$. FE is the $-\ln$ of the conditional probability that two similar σ-dimensional patterns remain similar for $\sigma + 1$. FE is the $-\ln$ of the conditional probability that two similar σ-dimensional patterns remain similar for $\sigma + 1$. Then,

$$\mathrm{FE(T)} = -\ln(\chi^{\sigma+1}(\mathrm{T})/\chi^{\sigma}(\mathrm{T})), \tag{5}$$

so that

$$\mathrm{FE(T)} = \ln(\chi^{\sigma}(\mathrm{T})/\chi^{\sigma+1}(\mathrm{T})). \tag{6}$$

With (6) taken into account, T_{optimum} can be obtained by

$$T_{\mathrm{optimum}} = \arg\ \min_{T}\left\{\left|\ln(\chi^{\sigma}(T)/\chi^{\sigma+})(T)\right|\right\}. \tag{7}$$

A pre-treatment can be implemented to improve the image quality globally ([38–40]). Section 5 details the proposed approach to compute a new $2D$ fuzzy entropy. Before

continuing with the discussion, the following remark is necessary.

Remark 2 FD (2) (together with (3) and (4)) leads to the calculation of $D^{\sigma}_{\bar{i},\bar{j},h,k} = D(\mathbf{A}^{\sigma}_{\bar{\mathbf{i}},\bar{\mathbf{j}}}, \mathbf{A}^{\sigma}_{\mathbf{h},\mathbf{k}})$. To consider (2) as a distance between images, we first need to define a suitable metric space and, on this space, verify that (2) represents a distance function. The following definition formalizes the metric space.

Definition 3 Let us consider the set X of all real-valued MFs, $m_{\mathbf{I}_{norm}}(\hat{a_{ij}})$, of images $\mathbf{I}_{norm}$ on $\hat{a_{ij}}$, defined and continuous on $\Omega = [0\ 1]$. Choosing the metric D (i.e. fuzzy divergence, FD), defined by (2), (3), and (4), we obtain $C(\Omega,\ D)$.

To ensure that D is a metric for $C(\Omega, D)$, we prove that FD satisfies all the axioms of the metric spaces. The following result holds.

Theorem 1 *Let us consider three generic fuzzy images* $F(\mathbf{I}_{norm})_j$, $j = 1, 2, 3$, *whose respective MF values are* $\hat{a_{ij}}$, $\hat{b_{ij}}$, $\hat{c_{ij}} \in X$. *Then*, (2) *satisfies the following four properties of the metric spaces*:

$$(1)\quad D(F(\mathbf{I}_{norm})_1, F(\mathbf{I}_{norm})_2) \geq 0; \tag{8}$$

$$(2)\quad D(F(\mathbf{I}_{norm})_1, F(\mathbf{I}_{norm})_2) = 0 \Leftrightarrow F(\mathbf{I}_{norm})_1 = F(\mathbf{I}_{norm})_2; \tag{9}$$

$$(3)\quad D(F(\mathbf{I}_{norm})_1, F(\mathbf{I}_{norm})_2) = D(F(\mathbf{I}_{norm})_2, F(\mathbf{I}_{norm})_1); \tag{10}$$

$$(4)\quad D(F(\mathbf{I}_{norm})_1, F(\mathbf{I}_{norm})_2) \leq D(F(\mathbf{I}_{norm})_1, F(\mathbf{I}_{norm})_3) + D(F(\mathbf{I}_{norm})_3, F(\mathbf{I}_{norm})_2). \tag{11}$$

Proof See Appendix A.

Remark 3 As shown in Appendix A, the proof of Theorem 1 is related to the images $F(\mathbf{I}_{norm})_1$, $F(\mathbf{I}_{norm})_2$, and $F(\mathbf{I}_{norm})_3$. However, the proof is still valid even if their portions are considered.

Remark 4 It is worth nothing that the total divergence, $D((\mathbf{I}_{norm})_w, \mathrm{FT})$, in (2), is computed by adding the two items, $\overline{D}((\mathbf{I}_{norm})_w, \mathrm{FT})$ and $\overline{D}(\mathrm{FT}, (\mathbf{I}_{\mathrm{norm}})_{\mathrm{w}})$, defined in (3) and (4), respectively. As declared in (10), the total divergence, $D((\mathbf{I}_{norm})_w, \mathrm{FT})$, obeys commutative law, while both the items $\overline{D}((\mathbf{I}_{norm})_w, \mathrm{FT})$ and $\overline{D}(\mathrm{FT}, (\mathbf{I}_{\mathrm{norm}})_{\mathrm{w}})$ do not obey the commutative law. In other words, $\overline{D}((\mathbf{I}_{norm})_w, \mathrm{FT}) \neq \overline{\mathrm{D}}(\mathrm{FT}, (\mathbf{I}_{\mathrm{norm}})_{\mathrm{w}})$ but $D((\mathbf{I}_{norm})_w, \mathrm{FT})$ satisfies the commutative law.

5 The Core of the Proposed Approach: A New Formulation of FE

As in [31], let us consider a generic $M \times N$ normalized image $\mathbf{I}_{norm}$ on which to define $\mathbf{A}^{\sigma}_{\bar{\mathbf{i}},\bar{\mathbf{j}}}$, which is the σ-length square window/pattern of origin $(\bar{i}, \bar{j})$. $\mathbf{A}^{\sigma}_{\bar{\mathbf{i}},\bar{\mathbf{j}}}$ represents the pixels in $\mathbf{I}_{norm}$ of indices ranging from $\bar{i}$ to $\bar{i} + \sigma - 1$ and from column $\bar{j}$ to $\bar{j} + \sigma - 1$. Matricially:

$$\mathbf{A}^{\sigma}_{\bar{\mathbf{i}},\bar{\mathbf{j}}} = \begin{pmatrix} \mathbf{I_{norm}}(\hat{\mathbf{a}}_{\bar{\mathbf{i}},\bar{\mathbf{j}}}) & .. & \mathbf{I_{norm}}(\hat{\mathbf{a}}_{\bar{\mathbf{i}},\bar{\mathbf{j}}+\sigma-\mathbf{1}}) \\ \mathbf{I_{norm}}(\hat{\mathbf{a}}_{\bar{\mathbf{i}}+\mathbf{1},\bar{\mathbf{j}}}) & .. & \mathbf{I_{norm}}(\hat{\mathbf{a}}_{\bar{\mathbf{i}}+\mathbf{1},\bar{\mathbf{j}}+\sigma-\mathbf{1}}) \\ .. & .. & .. \\ \mathbf{I_{norm}}(\hat{\mathbf{a}}_{\bar{\mathbf{i}}+\sigma-\mathbf{1},\bar{\mathbf{j}}}) & .. & \mathbf{I_{norm}}(\hat{\mathbf{a}}_{\bar{\mathbf{i}}+\sigma-\mathbf{1},\bar{\mathbf{j}}+\sigma-\mathbf{1}}) \end{pmatrix} \tag{12}$$

and $\mathbf{A}^{\sigma+1}_{\bar{\mathbf{i}},\bar{\mathbf{j}}}$ represents the $\sigma + 1$ square window. Additionally, $S_\sigma = (M - \sigma) \times (N - \sigma)$ denotes the total number of square windows in $\mathbf{I}_{norm}$ generated for both the σ and $\sigma + 1$ size. It is necessary that both the last σ-length row and column of $\mathbf{I}_{norm}$ are eliminated to ensure that $\mathbf{A}^{\sigma}_{\bar{\mathbf{i}},\bar{\mathbf{j}}}$ and $\mathbf{A}^{\sigma+\mathbf{1}}_{\bar{\mathbf{i}},\bar{\mathbf{j}}}$ can be defined for all indices $(1 \leq \bar{i} \leq M - \sigma,\ 1 \leq \bar{j} \leq N - \sigma)$. For $\mathbf{A}^{\sigma}_{\bar{\mathbf{i}},\bar{\mathbf{j}}}$ and its neighboring windows, $\mathbf{A}^{\sigma}_{\mathbf{h},\mathbf{k}}$, we quantify the distance between them, labeled by $D^{\sigma}_{\bar{i},\bar{j},h,k}$. By Theorem 1, $D^{\sigma}_{\bar{i},\bar{j},h,k} = D(\mathbf{A}^{\sigma}_{\bar{\mathbf{i}},\bar{\mathbf{j}}}, \mathbf{A}^{\sigma}_{\mathbf{h},\mathbf{k}})$.

Remark 5 In contrast to [31], the novelty introduced here involves the use of FD as the distance between $\mathbf{A}^{\sigma}_{\bar{\mathbf{i}},\bar{\mathbf{j}}}$ and $\mathbf{A}^{\sigma}_{\mathbf{h},\mathbf{k}}$ to take into account how far $\mathbf{A}^{\sigma}_{\bar{\mathbf{i}},\bar{\mathbf{j}}}$ is from $\mathbf{A}^{\sigma}_{\mathbf{h},\mathbf{k}}$ and vice versa.

The degree of similarity of each pattern is averaged to obtain

$$\chi^{\sigma}_{\bar{i}\,\bar{j}} = (S_\sigma - 1)^{-1} \sum_{h=1,k=1}^{h=M-\sigma,k=N-\sigma} D^{\sigma}_{\bar{i},\bar{j},hk}, \tag{13}$$

with $(h, k) \neq (\bar{i}, \bar{j})$, constructing

$$\chi^{\sigma} = (S_\sigma)^{-1} \sum_{\bar{i}=1,\bar{j}=1}^{\bar{i}=M-\sigma,\bar{j}=N-\sigma} \chi^{\sigma}_{\bar{i}\,\bar{j}}. \tag{14}$$

Analogously, for $\sigma + 1$,

$$\chi^{\sigma+1}_{\bar{i}\,\bar{j}} = (S_\sigma - 1)^{-1} \sum_{h=1,k=1}^{h=M-\sigma,k=N-\sigma} D^{\sigma+1}_{\bar{i}\,\bar{j},hk}, \tag{15}$$

with $(h, k) \neq (\bar{i}, \bar{j})$, to construct

$$\chi^{\sigma+1} = (S_\sigma)^{-1} \sum_{\bar{i}=1,\bar{j}=1}^{\bar{i}=M-\sigma,\bar{j}=N-\sigma} \chi^{\sigma+1}_{\bar{i}\,\bar{j}}. \tag{16}$$

As in (5), the FE of $\mathbf{I}_{norm}$ can be computed as

$$FE(\mathbf{I}_{norm}) = -\ln(\chi^{\sigma+1}/\chi^{\sigma}) = \ln(\chi^{\sigma}/\chi^{\sigma+1}). \quad (17)$$

This concludes the main steps of the proposed approach, which is based on the fuzzy MF concept. Considerable attention must be paid to its formulation because it is necessary to guarantee the smoothing properties of fuzzified images to ensure adaptive formulations, depending on the image to be fuzzified. The next section proposes a procedure to adaptively construct suitable fuzzy MFs by the joint application of a noise reduction approach and the entropy maximization principle.

6 What About the Fuzzy MF?

To fuzzify $\mathbf{I}_{norm}$, we use an S-shaped MF with good smoothing properties, depending on three shape parameters, s_1 s_2, and s_3, $s_1 < s_2 < s_3$, set adaptively. $\forall \hat{a_{ij}}$ in $\mathbf{I}_{norm}$, it is defined as

$$\begin{cases} m_{\mathbf{I}_{norm}}(\hat{a_{ij}}) = 0 \quad \text{if} \quad 0 \le \hat{a_{ij}} \le s_1, \\ m_{\mathbf{I}_{norm}}(\hat{a_{ij}}) = \dfrac{(\hat{a_{ij}} - s_1)^2}{(s_2 - s_3)(s_3 - s_1)} \quad \text{if} \quad s_1 \le \hat{a_{ij}} \le s_2, \\ m_{\mathbf{I}_{norm}}(\hat{a_{ij}}) = 1 - \dfrac{(\hat{a_{ij}} - s_3)^2}{(s_3 - s_2)(s_3 - s_1)} \quad \text{if} \quad s_2 \le \hat{a_{ij}} \le s_3, \\ m_{\mathbf{I}_{norm}}(\hat{a_{ij}}) = 1 \quad \text{if} \quad \hat{a_{ij}} \ge s_3. \end{cases}$$

In U, s_1 and s_3 are adaptively set by a noise reduction approach. Since s_2 is located around a gray level whose MF value falls around 1/2 (maximum dispersion of information), it is set it by the entropy maximization procedure (see Fig. 2).

6.1 s_1 and s_3: A Noise Reduction Approach

Starting from [40], we consider the gray-level distribution of $F(\mathbf{I}_{\text{norm}})$ and its histogram, Hist$\{\text{F}(\mathbf{I}_{\text{norm}})\}$. From the trend of the histogram of $F(\mathbf{I}_{\text{norm}})$ they are highlighted a number of peaks. Let g denote the number of these peaks indicated by Hist$\{\text{F}(\mathbf{I}_{\text{norm}})\}^1$,

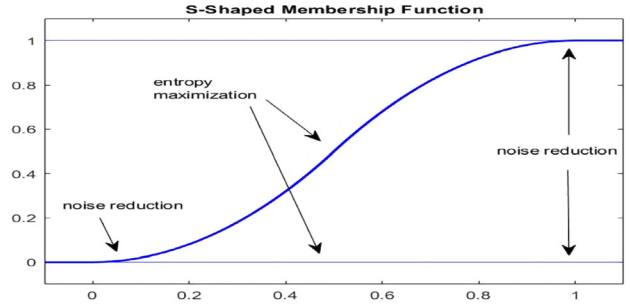

Fig. 2 S-shaped membership function: noise reduction and entropy maximization criteria to quantify the shape parameters adaptively

Hist$\{\text{F}(\mathbf{I}_{\text{norm}})\}^2$,..., Hist$\{\text{F}(\mathbf{I}_{\text{norm}})\}^g$. Then we compute

$$\frac{\sum_{i=1}^{g} H_{\text{ist\_max}}(m_{\mathbf{I}_{norm}}(\hat{a_{ij}}))\, m_{\mathbf{I}_{norm}}(\hat{a_{ij}})}{\sum_{i=1}^{g} m_{\mathbf{I}_{norm}}(\hat{a_{ij}})}, \quad (18)$$

which represents the height of the center of gravity of Hist$\{\text{F}(\mathbf{I}_{\text{norm}})\}$, taking into account the mutual position of Hist$\{\text{F}(\mathbf{I}_{\text{norm}})\}^{\text{j}}$, $j = 1, 2, \ldots, g$, in Hist$\{\text{F}(\mathbf{I}_{\text{norm}})\}$.

Remark 6 (18) is more complete than that obtained from the typical one $g^{-1}\sum_{j=1}^{g} H_{\text{ist\_max}}(m_{\mathbf{I}_{\text{norm}}}(\hat{a_{ij}}))$, which does not take into account the mutual position of Hist$\{\text{F}(\mathbf{I}_{\text{norm}})\}^{\text{j}}$, $j = 1, 2, \ldots, g$, in Hist$\{\text{F}(\mathbf{I}_{\text{norm}})\}$.

From the set of g peaks, we select $t \le g$ peaks larger than (18) (the others are less significant). From this reduced set of peaks, we select both maximum and minimum values: all pixels with a gray level lower than the minimum value are considered to be background, while all pixels with a gray level higher than the maximum value are similar to noise. Moreover, assuming that loss of information inside $F(\mathbf{I}_{\text{norm}})$ occurs in the neighborhood of the extremes of the range of their gray levels, it is appropriate to identify two particular gray levels, gl_1 and gl_2, with $gl_1 < gl_2$, so that the loss of information is equal to a fixed value $loss_{\text{information}}$: $\sum_{i=min(m_{\mathbf{I}_{norm}}(\hat{a_{ij}}))}^{gl_1} H_{ist}(i) = loss_{\text{information}}$, $\sum_{i=gl_2}^{max(m_{\mathbf{I}_{\mathbf{norm}}}(\hat{a_{ij}}))} H_{ist}(i) = loss_{\text{information}}$, and $0 < loss_{\text{information}} < 1$. Thus, both s_1 and s_3 are obtained as

$$\begin{cases} s_1 = \dfrac{\max\left(m_{\mathbf{I}_{norm}}(\hat{a_{ij}})\right) - \min\left(m_{\mathbf{I}_{norm}}(\hat{a_{ij}})\right)}{2} + \min\left(m_{\mathbf{I}_{norm}}(\hat{a_{ij}})\right), \\ s_3 = \dfrac{\max\left(m_{\mathbf{I}_{norm}}(\hat{a_{ij}})\right) + h_k}{2} + h_k. \end{cases}$$

Once s_1 and s_3 have been adaptively set, s_2 can be set by the entropy maximization principle. The following subsection details the idea.

6.1.1 s_2: Entropy Maximization Adaptive Procedure

Since $s_2 \in (s_1, s_3)$, the entropy of $F(\mathbf{I}_{\text{norm}})$, $E\left(F(\mathbf{I}_{\text{norm}})\right)$, will depend on $F(\mathbf{I}_{\text{norm}})$, and s_1, s_2, s_3, as well, such that $\min\left\{m_{\mathbf{I}_{\mathbf{norm}}}(\hat{a_{ij}})\right\} \le s_1 < s_2 < s_3 \le \max\left\{m_{\mathbf{I}_{\mathbf{norm}}}(\hat{a_{ij}})\right\}$. Furthermore, s_2 must be located so that its fuzzy membership degree is equal (or very close) to 0.5. In other words, s_2 represents the point of U at which the maximum FE occurs. Then, s_2 can be obtained as

$$\{s_2\}_{optimum} = \arg\max_{s_2} \left|\left(FE(\mathbf{I}_{\text{norm}}), s_1, s_2, s_3\right)\right|, \quad (19)$$

where $\left(FE(\mathbf{I}_{\text{norm}}), s_1, s_2, s_3\right)$ is computed using the proposed algorithm in Sect. 5.

Remark 7 We observe that s_2 has been computed through the criterion of maximization of entropy. This is due to the fact that $s_1 < s_2 < s_3$, and s_2 have a membership degree very close to 0.5 where, notoriously, the fuzzy entropy assumes a maximum value.

The procedure was qualitatively and quantitatively validated by using three experimental gray-level image datasets. The first database contains a set of gray-level EC maps that were established by subjecting steel plates to bi-axial loads, while the second dataset involves a set of gray-level thermal camera IR images of ballistic interest. Finally, gray-level electrospinning images are taken into account.

7 The Experimental Databases Description

7.1 ECs maps

This campaign of measurements was developed at our NDT & E Lab, in which $180 \times 180 \times 5$ m steel plates under symmetrical bi-axial loads (160 kN, with an uncertainty of about 5%) were investigated. Because of the microscopic structure of the material, the external load locally modifies the magnetic properties of the plates, whose degradation were investigated by analyzing the changes in the magnetic field $\mathbf{H}$ induced in the material when the deformations take place. The sensor was a FLUXSET® probe [41] whose pick-up voltage provides a measure proportional to the component of $|\mathbf{H}|$, parallel to the longitudinal axis of the sensor. Furthermore, both an *AC* sinusoidal exciting field (1 kHz) and an electric current (120 mA RMS) were applied. With regard to the driving signal, a triangular shape at a frequency of 100 kHz with a $2Vpp$ amplitude was chosen. After the symmetrical bi-axial load application, the specimens were investigated by obtaining four $2D$ signals that are representative of the real part, the imaginary part, the module, and the phase of the pick-up voltage (mV) at each point of the surface of the specimen. For our purposes, each $2D$ EC map is represented as a gray-scale image (one of them is depicted in Fig. 3a), and the considered database contains 75 images that show the real part of the pick-up voltage.

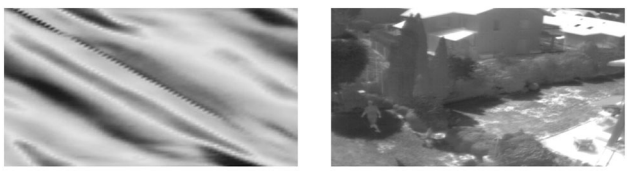

(a) (b)

Fig. 3 **a** A typical EC map. **b** An example of IR image

7.2 Thermal Camera IR Images

IR thermography is a non-destructive diagnostic technique that measures the IR emitted by a body to determine its surface temperature. According to the Stefan-Boltzmann law, the amount of IR emitted depends on the fourth power of the absolute surface temperature of an object. The employed dataset, available online for free at https://www.flir.com/oem/adas, contains more than 14K total thermal 8-bit images, with more than 10K from short video segments and random image samples. The captured images were recorded at 30 Hz, with sequences sampled at 2 (or 1) frame per second. In the experiment, we chose IR images with presence of a human in thick vegetation (100 images). An Example of IR images is shown in Fig. 3b.

7.3 Electrospinning Images

ES is a process by which a solution or molten polymer can be spun into small-diameter fibers (3 nm and 4 μm) by a high electric potential [37] to obtain fibers with high surface area with respect to the volume and superior mechanical performances compared with any other known form of material. The spinneret is connected to a syringe containing the melted polymer, which passes through the spinneret with a constant and controllable flow. When a high potential difference is applied between the syringe capillary and the collector (usually between 1 and 30 kV), a drop of the extruded polymer is formed. As the electrical tension increases, the drop undergoes a repulsive force, so it is distorted into a conical shape [42–45]. As soon as the electric field exceeds a certain value, the electrostatic forces prevail over the surface tension of the drop and cause the expulsion of a jet of liquid. The solvent traveling toward the evaporate collector increases the surface charge of the jet-inducing instability that the whipping motion undergoes, leading to the formation of a thin wire. The charged fiber is attracted by the collector and goes on to deposit itself over it as a non-woven fabric with a random orientation. Usually, poly-vinyl-acetate (with an average molecular weight of 170×10^3 g/mol) and ethanol are employed as the polymer and solvent, respectively. If the morphology of the produced nanofiber is analyzed by means of a Phenom Pro-X scanning electron microscope (SEM), it is possible to produce gray-level SEM images. In this work, the SEM image dataset proposed in [37] was used. In particular, it consists of 75 images of homogeneous nanofibers (HNFs). All images are 128×128. As an example, Fig. 4 shows HNF SEM image.

The proposed approach was applied to all figures of the three above-mentioned databases. Section 8 provides a brief overview of typical I- and II-order edge detectors that

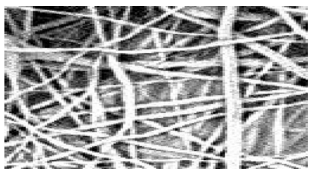

Fig. 4 An example of HNF SEM image

were used in this work to compare the results obtained by using the proposed procedure.

8 First-Order Edge Detection Procedures

8.1 The Roberts Procedure

Roberts operators are based on the implementation of diagonal differences [1]. Taking into account a region 3×3 of $\mathbf{I}$, $[z_1\ z_2\ z_3;\ \ z_4\ z_5\ z_6;\ \ z_7\ z_8\ z_9]$, the diagonal differences, $(\mathbf{I})_\mathbf{i} = \mathbf{z_9} - \mathbf{z_5}$ and $(\mathbf{I})_\mathbf{j} = \mathbf{z_8} - \mathbf{z_6}$, are implemented by means of 2×2 template filtering. However, they are not able to calculate the direction because they are not symmetrical with respect to the central point, so one applies 3×3 templates while considering the nature of the data on opposite sides with respect to the central point.

8.2 The Prewitt and Sobel Procedures

The approximations of $(\mathbf{I})_\mathbf{i}$ and $(\mathbf{I})_\mathbf{j}$, with 3×3 templates, are given by $(z_7 + z_8 + z_9) - (z_1 + z_2 + z_3)$ and $(z_3 + z_6 + z_9) - (z_1 + z_4 + z_7)$, respectively. The difference between the third and the first row of the 3×3 region approximates $(\mathbf{I})_\mathbf{i}$, while the difference between the third and the first column approximates $(\mathbf{I})_\mathbf{j}$. Both $(\mathbf{I})_\mathbf{i}$ and $(\mathbf{I})_\mathbf{j}$ can be implemented by filtering with two templates that represent the Prewitt operators. Instead, considering $2z_8$ and $2z_2$, a slight smoothing of $\mathbf{I}$ is introduced. The templates represent Sobel operators [1].

9 Second-Order Edge Detection Procedures

In an image, the intensity variations depend on the image scale; thus, their identification requires the use of operators with higher orders [1]. In addition, a sudden intensity change produces either a peak along the first derivative or a zero-crossing in the second derivative. To build an operator, it is necessary that: (1) it represents a differential operator able to calculate digital approximations of first and second derivative, $\forall (i,j) \in \mathbf{I}$; (2) it is adjusted to act on each selected scale, so larger operators can be used to identify blurred edges, and small operators identify poorly visible details [1, 17].

9.1 Laplacian of Gaussian (LoG) and Zero-Cross Approaches

The best operator with respect to both conditions (1) and (2) is $\nabla^2 G(i,j)$, where $G(i,j) = \mathrm{e}^{\frac{i^2+j^2}{\mathrm{std}^2}}$, with std denoting the standard deviation. Combining $\nabla^2(\cdot)$ with $G(i,j)$, we achieve $\nabla^2 G = \left[\frac{i^2+j^2-2\mathrm{std}^2}{\mathrm{std}^4}\right] \mathrm{e}^{-\frac{i^2+j^2}{2\mathrm{std}^2}}$, which represents the LoG. It easy to prove that the zero-crossings of the LoG occur in $i^2 + j^2 = 2\mathrm{std}^2$. Then, templates are built by sampling $\nabla^2 G(i,j)$ and scaling its coefficients so that they give a zero-sum. Alternatively, it is possible to sample $\nabla^2 G(i,j)$ to the desired size and convolve the results with a Laplacian template. By convolving $\mathbf{I}$ with a template whose coefficient gives a zero-sum, one obtains results with elements that give a zero-sum to satisfy the requirement that the sum of the LoG filter coefficient be zero. The algorithm performs the convolution of $\nabla^2 G = \left[\frac{i^2+j^2-2\mathrm{std}^2}{\mathrm{std}^4}\right] \mathrm{e}^{-\frac{i^2+j^2}{2\mathrm{std}^2}}$ with $\mathbf{I}$; after that, it determines the edge position by computing the zero-crossing (using a 3×3 pixel-centered neighborhood so that the signs of at least two of its opposite neighboring pixels must be different) [1, 18].

9.2 The Canny Approach

This approach uses the calculation of the variations for the search of the function to optimize a given functional defined as the sum of four exponential terms or by the first derivative of a Gaussian function. If the algorithm uses a filter based on a derivative before a Gaussian, the results are affected by the noise in $\mathbf{I}$, that needs a pre-treatment based on convolution with a Gaussian filter to obtain a slightly blurred image in which no pixel is significantly affected by noise. After that, four different filters identify the horizontal, vertical, and diagonal contours in $\mathbf{I}$. The direction relative to the filter that provides the most value is assumed to be valid on each resulting pixel. This direction, combined with the value obtained by applying the filter, corresponds to that in which there is the maximum brightness gradient for each point of $\mathbf{I}$. Only the points corresponding to local maxima (points at which the derivative of the gradient is zero) are considered to belong to an edge. Finally, contour extraction is performed with a thresholding procedure with hysteresis. In particular, two thresholds are defined (one high and one low that justify the reference to hysteresis) and compared with the gradient at each point. If the gradient is less than the low threshold, then the point is discarded; if, instead, it is greater than the

high threshold, the point is considered to belong to an edge. Finally, if the gradient is between the two thresholds, the point is accepted as an edge if it is contiguous to a previously accepted point. For more details, see [1, 17].

9.3 The Otsu-Canny Approach

The Otsu operator [14], also-called the maximum class square error method, is a self-adapting threshold determination method solving the Canny operator's problem, which is that it is unable to select the high and low thresholds adaptively according to the image characteristics [14]. The Otsu operator uses the thresholds to divide the image into background and target. The best threshold occurs when the difference between the background and the target is greater. In other words, the maximum variance between the background and target classes is obtained. The procedure for obtaining the optimal threshold value for the Otsu operator is as follows. If T is the segmentation threshold between the background and targe of an image, the grayscale range of the image is $G = [0, L-1]$, while the probability of each grayscale is indicated by p_i. Then, T divides the image into two cateories: $G_0 = [0, T]$ and $G_1 = [T+1, L-1]$. Thus:

1. *the probability of* G_0 *and* G_1 *are* $\alpha_0 = \sum_0^T p_i$ *and* $\alpha_i = 1 - \alpha_0$, *respectively;*
2. *the average gray values of the two categories* G_0 *and* G_1 *are* $\mu_0 = \frac{\mu_T}{\alpha_0}$ *and* $\mu_1 = \frac{\mu - \mu_T}{1-\alpha_0}$, *respectively, in which* $\mu = \sum_0^{L-1} i \times p_i$ *and* $\mu_T = \sum_0^T i \times p_i$;
3. *the cluster variance of the two categories is computed as follows:*

$$\eta^2(T) = \alpha_0(\mu_0 - \mu)^2 + \alpha_1(\mu_1 - \mu)^2 - \alpha_0\alpha_1(\mu_0 - \mu_1)^2. \tag{20}$$

Finally, to obtain $T_{optimal}$ it is sufficient to compute $\max(\eta^2(T))$.

The procedure proposed in this paper is reasonable to apply if the fuzziness content of each processed image, quantified by suitable IoFs, assumes appreciable values. In Sect. 10 we presents a new approach to evaluate IoFs, based on FD formulation, that are useful for our purposes.

10 Suitable Indexes of Fuzziness (IoFs)

An IoF of $F(\mathbf{I}_{norm})$, defined in [17], is depending on $d^p(F(\mathbf{I}_{norm}), \overline{F(\mathbf{I}_{norm})})$, which represents a p-distance between $F(\mathbf{I}_{norm})$ and its nearest ordinary image $\overline{F(\mathbf{I}_{norm})}$, whose MF is defined as in [17]. Moreover, $IoF(F(\mathbf{I}_{norm})) \in [0\ 1]$. The higher the value of $IoF(F(\mathbf{I}_{norm}))$, the greater the fuzzy distance of $F(\mathbf{I}_{norm})$ from its nearest crisp image. In addition, $IoF(F(\mathbf{I}_{norm}))$ can be considered a fuzziness measure in $F(\mathbf{I}_{norm})$. To underline the fuzziness of the problem, since FD is a distance between fuzzy images (Appendix A) that takes into account how far one image is from the other and vice versa, we define *IoFs* as follows.

Definition 4 With $D^p\left(F(\mathbf{I}_{norm}), \overline{F(\mathbf{I}_{norm})}\right)$ denoting the FD between $F(\mathbf{I}_{norm})$ and $\overline{F(\mathbf{I}_{norm})}$, in which the differences among MF values are considered to be a power of $p \in \mathbb{N} - \{0\}$, we define a new IoF as

$$IoF(F(\mathbf{I}_{norm})) = 2(M \times N)^{-\frac{1}{p}} \cdot \left(D^p\left(F(\mathbf{I}_{norm}), \overline{F(\mathbf{I}_{norm})}\right)\right)^{1/p}, \quad p \in \mathbb{N} - \{0\}. \tag{21}$$

From which the linear and quadratic IoFs are

$$(IoF)_p = 2(M \times N)^{-\frac{1}{p}} \cdot \left(D^p\left(F(\mathbf{I}_{norm}), \overline{F(\mathbf{I}_{norm})}\right)\right)^{\frac{1}{p}}, \quad p = 1, 2. \tag{22}$$

Moreover, Yager's Measure, defined as

$$(YM)_p = 1 - (M \times N)^{-\frac{1}{p}} \cdot \left(D^p\left(F(\mathbf{I}_{norm}), \overline{F(\mathbf{I}_{norm})}\right)\right)^{\frac{1}{p}}, \quad p = 1, 2, \tag{23}$$

can be used.

Once the proposed procedure is applied to images, we use QAMs to evaluate their quality performances. Section 11 details some reference and nonreference QAMs suitable for our purposes.

11 QAMs for ED Procedures: Reference & Nonreference ED Measures

11.1 Reference ED Measures: Mean Square Error (MSE), Mean Absolute Error (MAE), Structural Similarity Measure (SSIM)

The simplest way to evaluate the performance of an edge detector is to quantify the distance (or the similarity) between the segmented image, $\mathbf{I}(\mathbf{a_{ij}})$, and an image, $\mathbf{I}(\mathbf{b_{ij}})$, whose edges have been optimally detected [1, 17]. Two simple statistical indexes are MSE and MAE. It is worth noting that, in this work, the distances between two fuzzified images, $F(\mathbf{I}_{norm})_1$ and $F(\mathbf{I}_{norm})_2$, were quantified by FDs, $D(F(\mathbf{I}_{norm})_1, F(\mathbf{I}_{norm})_2)$, in order to take into

account how far $F(\mathbf{I}_{norm})_1$ is from $F(\mathbf{I}_{norm})_2$, and vice versa. Then:

$$MSE = (M \times N)^{-1} \cdot \sum_{i=1}^{N} \sum_{j=1}^{N} \Big(D(F(\mathbf{I}_{norm})_1(i,j), F(\mathbf{I}_{norm})_2(i,j)) \Big)^2, \quad (24)$$

$$MAE = (M \times N)^{-1} \cdot \sum_{i=1}^{N} \sum_{j=1}^{N} \Big| D(F(\mathbf{I}_{norm})_1, F(\mathbf{I}_{norm})_2) \Big|. \quad (25)$$

SSIM is based on the fact that the human visual system extracts structural information to define the similarity between two images, $\mathbf{I_1}$ and $\mathbf{I_2}$, as a function of luminance $l(\mathbf{I_1}, \mathbf{I_2})$, contrast $c(\mathbf{I_1}, \mathbf{I_2})$, and structure $s(\mathbf{I_1}, \mathbf{I_2})$ (depending on statistical parameters). In other words, $SSIM = l(\mathbf{I_1}, \mathbf{I_2})\mathbf{c}(\mathbf{I_1}, \mathbf{I_2})\mathbf{s}(\mathbf{I_1}, \mathbf{I_2})$. *SSIM* is applied to non-overlapping windows. Thus, the mean of the SSIM values over the entire image is used to indicate the similarity between two images. For our goals, $\mathbf{I_1}$ and $\mathbf{I_2}$ represent fuzzified images, while they represent normalized images for the remaining approaches used for comparison [1].

11.2 Nonreference ED Measures: Yitzhaky/Peli Measure and Panetta Measure

Yitzhaki and Peli automatically estimate the background truth map by examining the corresponding threshold receiver operating characteristics curve, starting from a range of detection results and obtained from different detection parameter sets. The single parameter set is identified from the edge map that is most similar to the estimated background truth edge. The Yitzhaky procedure, which uses the N results obtained from N applications of an edge detector using N different parameters, selects the optimal operating parameters by a specific criterion. For our purposes, if the edge detector used is of the crisp type, the images used are the normalized raw images. Otherwise, using the proposed algorithm, the images to be processed are the fuzzified ones ([33]). The approach proposed by Panetta et al. [33] is structured in three steps: (1) generation of a gray-scale edge map; (2) reconstruction procedure; (en in dense shadow areas (3) use of a similarity measure. Starting from an extracted edge map, a continuous edge map is generated by a morphological dilation to contain information from the original image and multiplied with the original image to achieve a new gray-scale edge map. To establish an effective reconstruction procedure with a good balance and robustness to noise, Panetta et al. [33] used a weighted α that was trimmed on the basis of the parameter α (tuned for different applications). The reconstructed image was compared with the original image by a similarity measure on the basis of the Gradient SSIM index [33], which compares both images and their gradient to produce a similarity measure with good performance, even when images are affected by distortions (for details, see [33]).

Remark 8 It is worth nothing that *MSE*, *MAE* and *SSIM* are reference ED Measures. They measure a sort of distance of an edge detected image from another one considered as excellent. Here, Canny's procedure with Otsu operator provides the best results in terms of edge detection (that is, the method that most details the edges in an image) so that the images achieved by this procedure represent the reference images from which to compute *MSE*, *MAE* and *SSIM*, unlike the Yitzhaki & Peli and Panetta measures which are non-reference ED measures for which they do not require reference images.

12 Numerical Results

For each image, $(IoF)_1$, $(IoF)_2$, $(YM)_1$, and $(YM)_2$ values were plotted in Figs. 5, 6 and 7 noting that the indexes do not assume trends suggesting us that behaviors can be linked to each category of images. However, the high values obtained confirmed the high content of fuzziness in each image; so that, all images were edge-detected with performances considered satisfactory because almost equivalent to the edge detection results achieved by means of Canny's procedure (with Otsu operator). These results were confirmed through the implementation of the references/non references QAMs.

12.1 Edge Detection of ECs maps

The proposed procedure identifies the transversal lines at which the most significant gradients occur; this is in

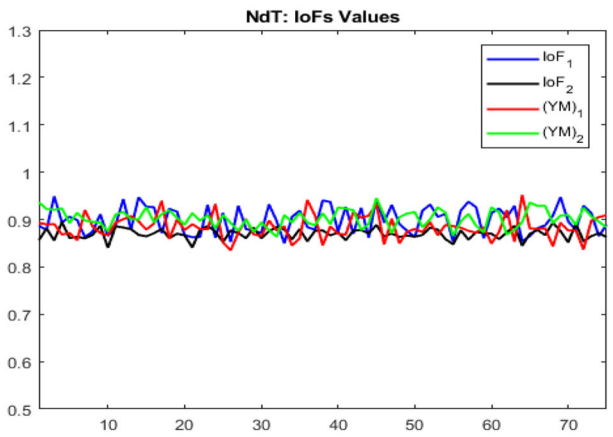

Fig. 5 IoF for EC maps

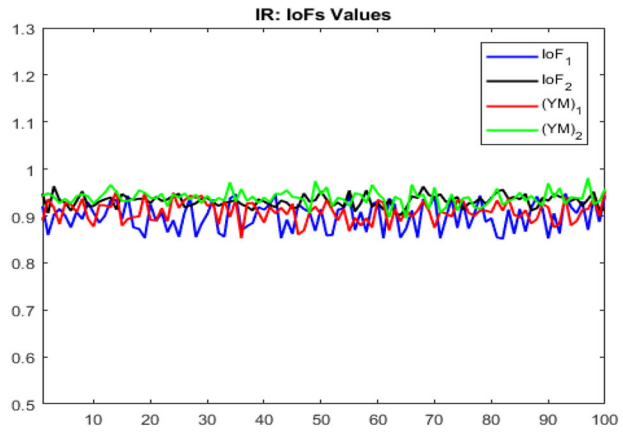

Fig. 6 IoF for IR images

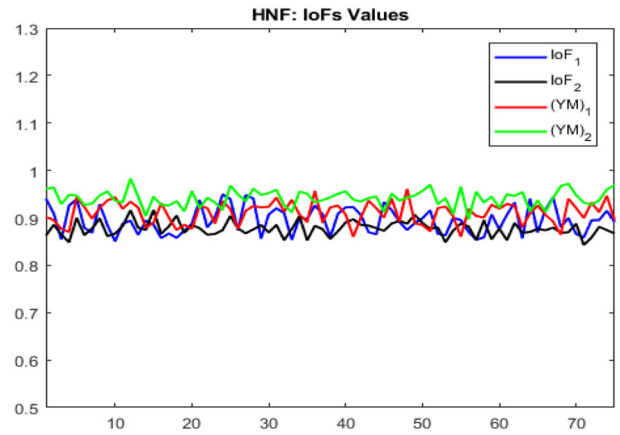

Fig. 7 IoF for HNF images

contrast to the I-order techniques, which are unsuccessful. As regards the results obtained with the II-order techniques, LoG and Zero-Cross identify the main line of the pick-up voltage gradient (secondary diagonal, which is considered the most dangerous since it is linked to high mechanical stress states) but do not identify less intense gradients, which are necessary to define the health of the plate. Completely different are the results obtained with the Canny operator (with and without Otsu operator), which identifies all the gradients of the pick-up voltage to provide a complete and exhaustive edge detection. Therefore, qualitatively, the performances obtained with the proposed approach can be considered almost equivalent to those obtained with the Canny procedure with Otsu operator. As an example, Fig. 8a depicts the ED of an EC map (Fig. 3a) by the proposed procedure, showing that the performance obtained is very close to that obtained with the Canny & Otsu approach (Fig. 8g and h). Figure 8b–d demonstrate the disappointing results from applying the I-order procedures, while Fig. 8e and f, relating to the performance of the LoG and Zero-Cross operators, respectively, confirm

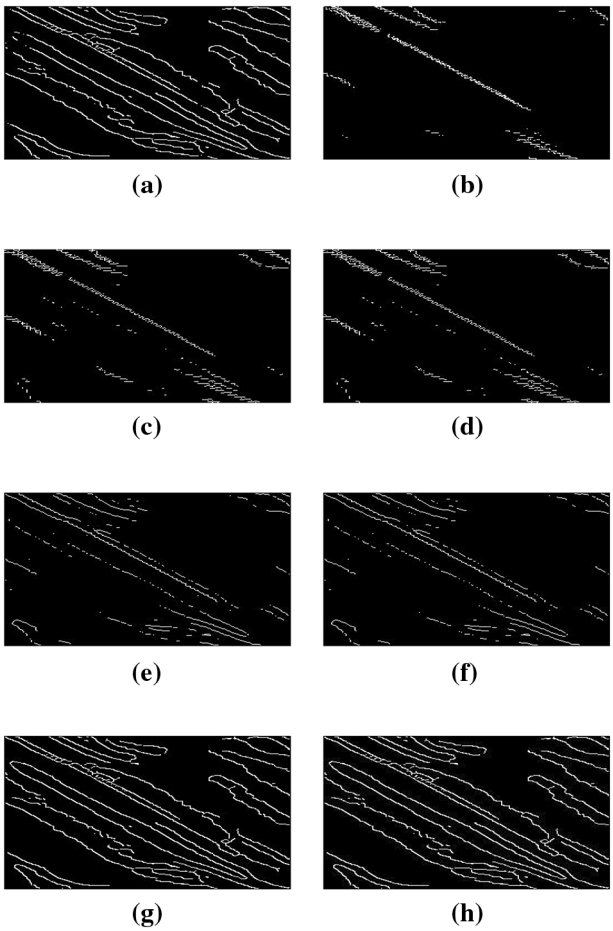

Fig. 8 EC map: ED performed by **a** the proposed approach; **b**, **c**, and **d** by the Roberts, Prewitt, and Sobel approaches; **e**, **f**, **g** and **h** by the LoG, Zero-Cross, Canny and Canny & Otsu procedures

that a good detection is achieved only of the diagonal of greater stress.

Quantitatively, the situation does not change in substance and agrees with the qualitative analysis. In fact, with the image obtained using the Canny operator (qualitatively, it is the most complete in highlighting all the edges) used as a reference, all the merit curves relating to the reference QAMs are traced (see Fig. 9a–c), highlighting that the proposed procedure demonstrates a performance that is very close to that obtained by the Canny operator. To further confirm the similarity between the performance of the proposed procedure and the performance obtained with Canny's operator, the merit curves for Yitzhaky's and Panetta's measures were determined (Fig. 9d and e), and the similarity is evident. Furthermore, it is worth noting that the nonreference QAMs differentiate the performance between operators with greater clarity compared with the reference measures, which, while showing the similarity in performance between the proposed procedure and Canny's approach, do not provide differentiation that is sufficient to

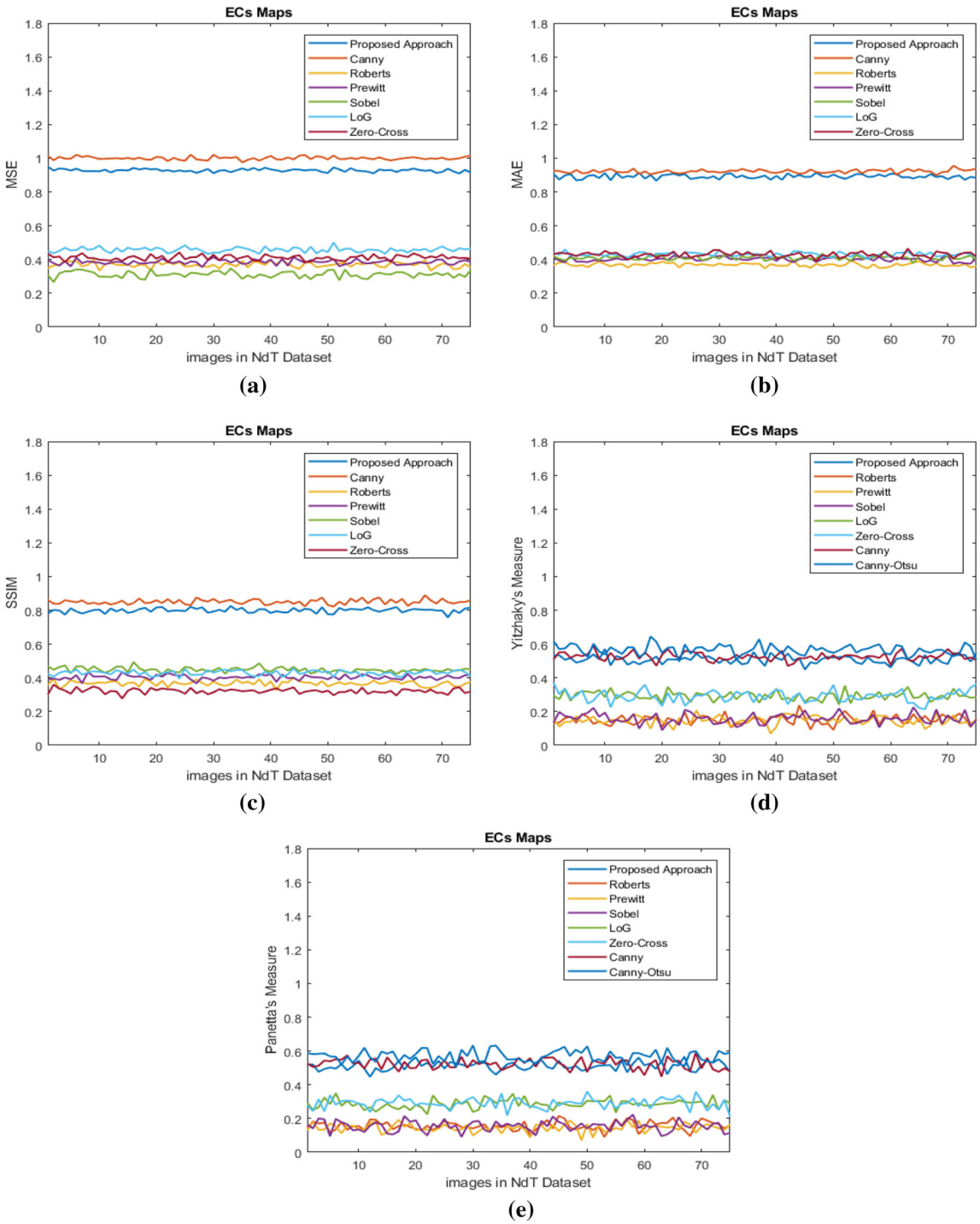

Fig. 9 QAMs for EC maps: **a** MSE, **b** MAE, **c** SSIM, **d** Yitzhaky's measure, **e** Panetta's measure

assess the differences in the performance of other procedures.

12.2 Edge Detection of IR Images

The proposed approach is able to detect, with a good level of detail, the presence of humans in shaded areas with thick vegetation. The Roberts, Prewitt, and Sobel techniques fail to detect the presence of humans while detecting, with a fair degree of detail, edges related to other areas of the images. The LoG and Zero-Cross, which show better performance compared with the operators of the first order, are able to detect the presence of humans but with an insufficient level of detail. For the EC maps, the Canny operator

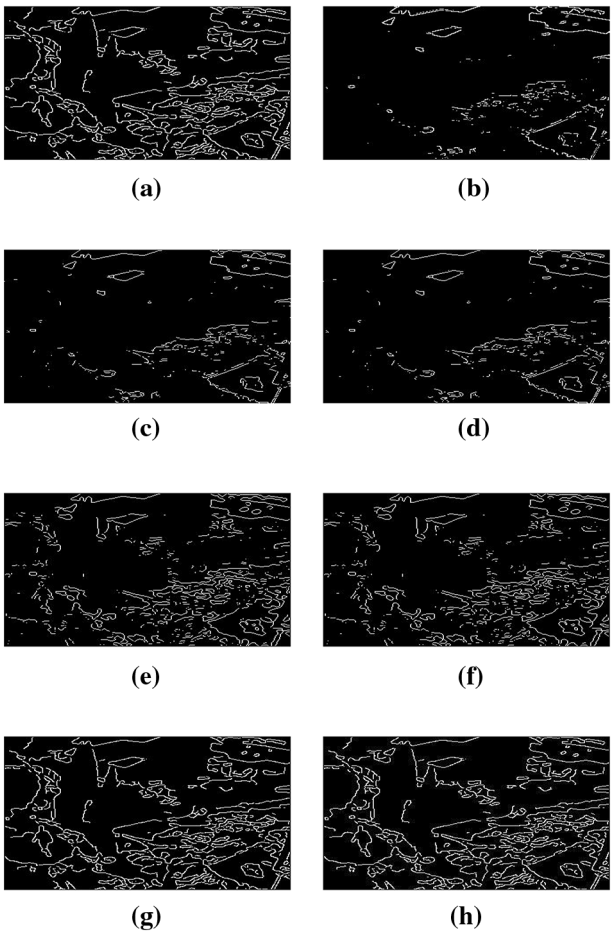

Fig. 10 IR image: ED performed by **a** the proposed approach; **b**, **c**, and **d** by the Roberts, Prewitt, and Sobel approaches; **e**, **f**, **g** and **h** by the LoG, Zero-Cross, Canny and Canny & Otsu procedures

(with and without Otsu procedure) exhibits excellent performance by detecting the presence of humans even in dense shadow areas (Fig. 10g and h). Additionally, for this type of image, the performances of the proposed approach and the Canny method can be considered similar. As an example, Fig. 10a shows the performance of the proposed approach as an elaboration of Fig. 3b, highlighting the good comparability to the performance obtained with the Canny operator (see Fig. 10g). The Roberts, Prewitt, and Sobel procedures, as shown in Fig. 10b–d, do not exhibit acceptable performances. However, Fig. 10e and f, as II-order operators, detect, albeit weakly, the presence of humans.

The qualitative analysis was confirmed by tracing the merit curves of the reference metrics (Fig. 11a–c, referred to the image obtained with the Canny operator) and non-reference metrics (Fig. 11d and e), highlighting the similarity between performances of the proposed approach and the Canny procedure. It is worth noting that, contrary to the results obtained with the EC maps, given the wealth of details contained in the images analyzed and the fact that they do not have the same panoramic scenarios, the figures of merit are erratic. However, despite the presence of these oscillations, the qualitative differences in performance of the edge detectors are highlighted as a result of the location of the individual curves in certain ranges of metric values.

12.3 Edge Detection of HNF SEM Images

The proposed approach applied on HNF SEM images is satisfactory since the detected textures are extremely detailed (Fig. 12a) and equivalent to those obtained with the Canny procedure (Fig. 12g and h). The LoG and Zero-Cross procedures (Fig. 12e and f) offer good results so they are still attractive in this type of image; while the I-order techniques produce poor performances (Fig. 12b–d).

The curves of merit (Fig. 13a–e) confirm the results highlighted by the qualitative analysis. One more time, the curves of merit highlight the different performances because of the distinct ranges of metric values, each derived from edge detectors with equivalent performance. Further, the presence of oscillations in the curves of merit is due to the high differentiation of the images subjected to processing. However, the amplitudes of these oscillations are reduced compared with the IR images because the textures of the HNF SEM images are similar to each other, quantitatively confirming that which is highlighted by the qualitative analysis.

13 Conclusions

In this paper, a new approach based on the joint use of FE and FD is presented and tested for solving the ED problems for gray-level images characterized by uncertainty, imprecision, or both. First, it is proved that a particular FD formulation is also a distance between images. With a well-known FED approach (Chaira and Ray [17]) and FE procedure (Silva [31]) used as a basis, the proposed procedure acts on [17] in its thresholding step by implementing the modified FE [31], in which the distances between images are computed by means of FD. In addition, the new approach for image fuzzification presented in this paper, based on S-shaped membership functions in which the shape parameters have been selected by FE and noise reduction, unlike other well-known procedures [17, 19], allows us to adaptively fuzzify the images under study. This new formulation of FE by FD, unlike Silva's procedure [31] and other well-established approaches [16, 24, 28, 29], allows us to take into account how far an image is from another one and vice versa. The proposed procedure was tested on three kinds of images (EC maps,

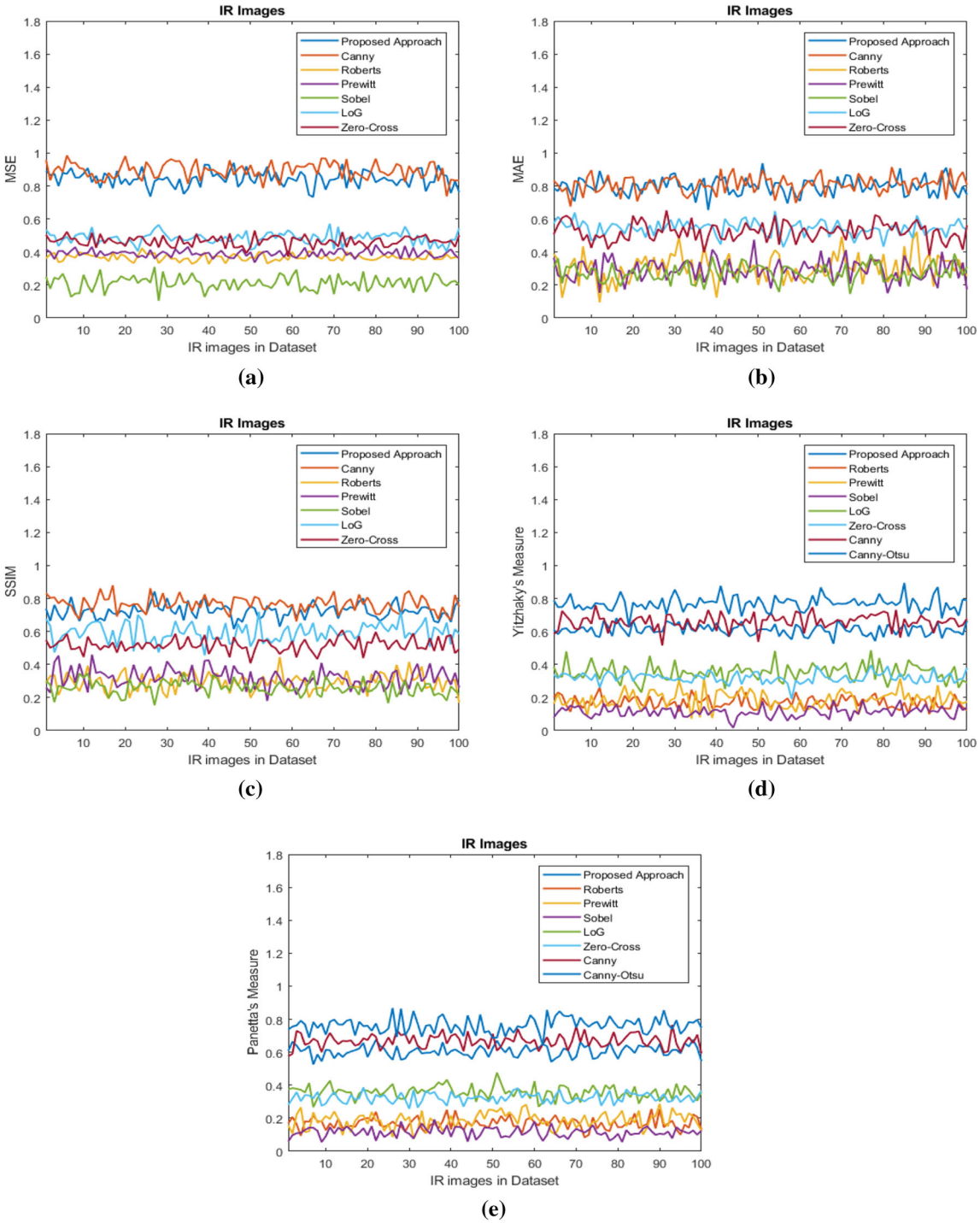

Fig. 11 QAMs for IR images: **a** MSE, **b** MAE, **c** SSIM, **d** Yitzhaky's measure, **e** Panetta's measure

IR images, and, finally, ES images after their fuzziness levels were checked by new suitable IoFs here presented), and the obtained results were compared with those achieved by well-established crisp techniques based on I- and II-order derivatives [18, 19]. The results are considered to be highly encouraging because the "ad hoc" formulated reference QAMs confirm, for all images analyzed, that the performance of the proposed procedure is almost equivalent to the performance of the most popular edge detector, namely, Canny's edge detector (with & without Otsu procedure). In particular, the proposed QAM values, unlike other existing and well-established metrics [17, 18, 32], fall within certain numerical intervals that are distinct from each other, even if depending on the applied ED procedure.

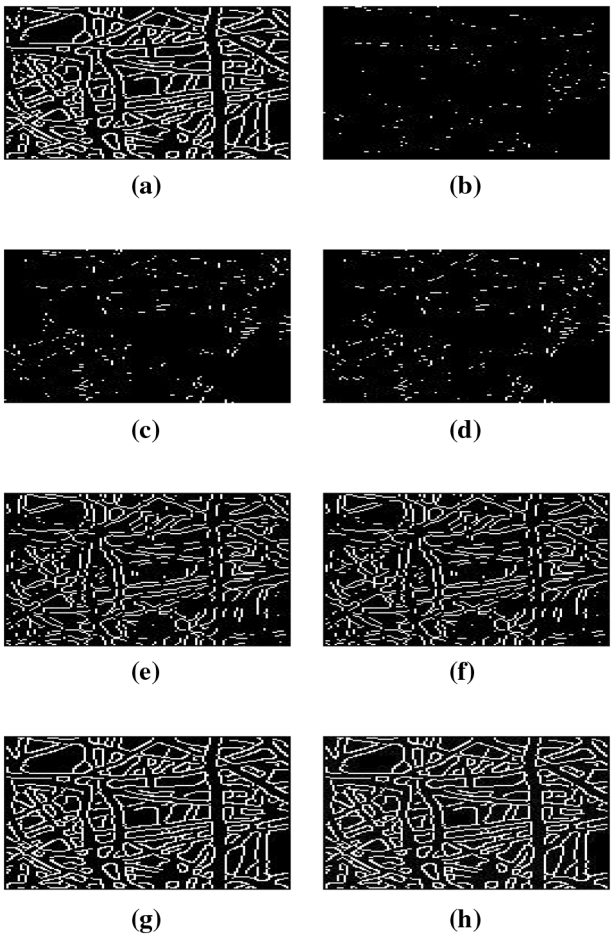

Fig. 12 HNF SEM image: ED performed by **a** the proposed approach; **b**, **c**, and **d** by the Roberts, Prewitt, and Sobel approaches; **e**, **f**, **g** and **h** by the LoG, Zero-Cross, Canny and Canny & Otsu procedures

Therefore, this suggests that, for the same images, different conditions lead to different trends of merit curves. This is more intuitive if we refer to the EC maps, in which different bi-axial loads result in different EC maps and, therefore, different curves of merit. Thus, in this case, the curves of merit can be used to classify classes of bi-axial loads, even though this is favored by the fact that the values of the QAMs obtained for the EC maps have reduced fluctuations with respect to the QAM values achieved when IR and ES images were analyzed. The proposed method is preferable to the Canny method [17–19, 45] since the Canny procedure (with or without Otsu thresholding) has a considerably higher computational complexity (it is a II-order differential method). Furthermore, the Canny procedure does not take into account any fuzziness content of each image. In other words, the performance of the Canny procedure (with or without Otsu thresholding) is slightly higher than the proposed procedure, so that, for real-time application, the proposed approach is preferred as it is characterized by a lower computational complexity.

14 Perspectives

This work has to be considered as a forerunner for future insights. The following remarks can be considered as a starting point for future research. In particular:

- in this paper, the FD exploited was selected from a large number of formulations which, on the one hand, met the four axioms as detailed in Definition 1 and, on the other, could be considered as a measure of distance between fuzzified images. In this framework, it would be appropriate to develop an adaptive construction technique of FDs that must meet regularity requirements and, moreover, ensure both existence and uniqueness. Finally, it is imperative that the choice of the FD construction should be automated and made adaptive according to the characteristics of the images under study;
- an important aspect of the proposed approach concerns the fuzzification of images. The use of the S-shaped MF, built using criteria based on entropy maximization and noise reduction as well, has provided good results as the totally automated procedure is adaptive and sets the shape parameters according to the image under study. However, it would be appropriate to develop in the future a more refined technique for noise reduction taking into account the different types of corruption that two-dimensional signals can suffer;
- crucial point of the proposed procedure concerns the formulation of fuzzy entropy. The proposed procedure, even if it is adaptive, does not take into account the statistics of the image under study (and its portions). In the future it is worth investigating this aspect in order to formulate entropies more adherent to the morphology of an image;
- it is worth noting that, to fully evaluate an ED procedure, the number of edge detected would need to be quantified. However, this is possible when the analyzed images do not have jagged edges. The analyzed images, excluding some details in each of them, have highly jagged edges so the quantification of the edges is impractical. So, in the near future, it would be desirable to develop an edge detected quantifier starting from the number of pixels detected.

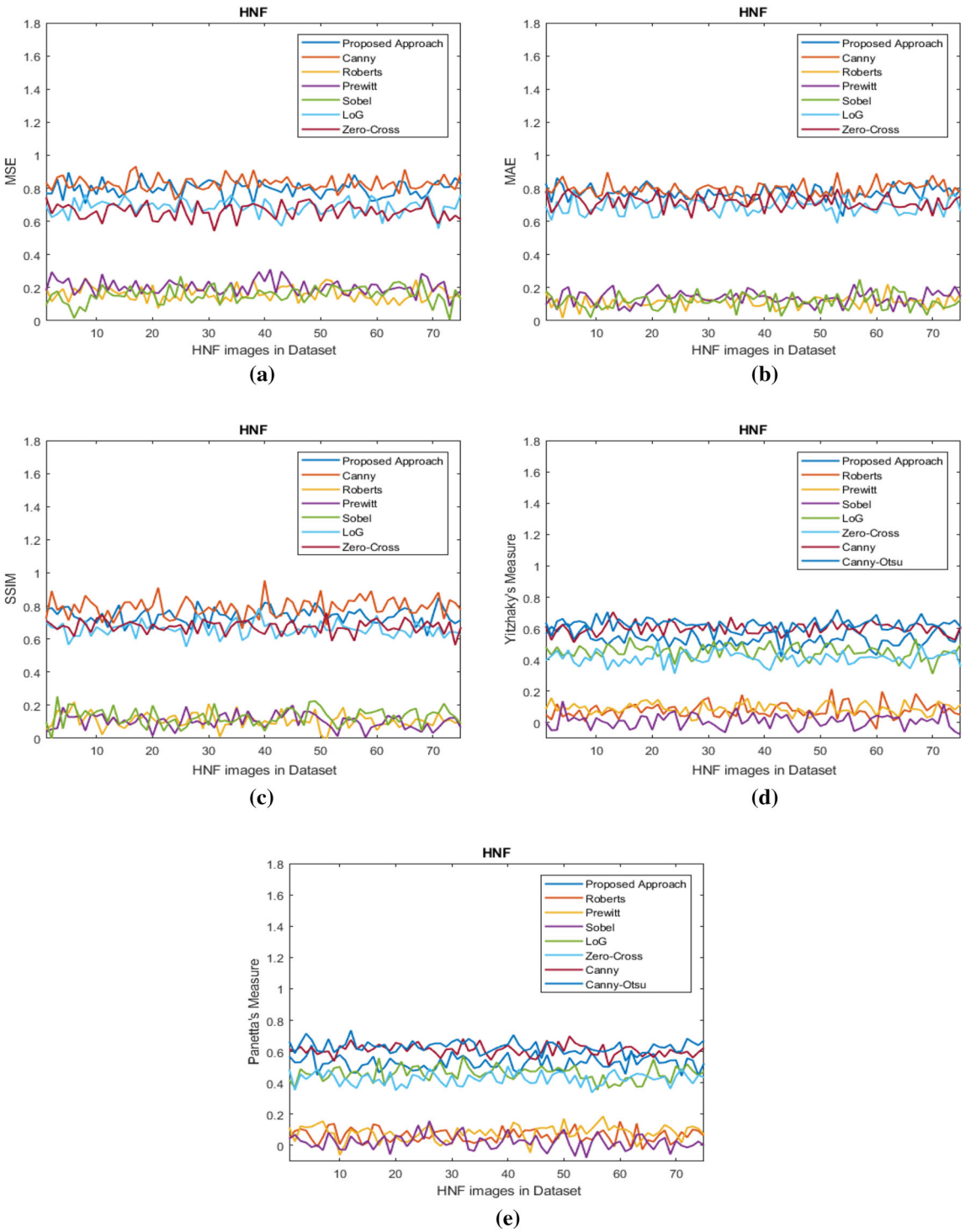

Fig. 13 QAMs for HNF images: **a** MSE, **b** MAE, **c** SSIM, **d** Yitzhaky's measure, **e** Panetta's measure

– the algorithm proposed in this paper is related to the edge detection of grayscale images. It therefore seems natural to extend the procedure to RGB images. Currently, in our Lab, the extension of the proposed procedure to color images is at an advanced stage;

– last, but not least, the new formulations of nonreference metrics presented in this work have provided results that operate, for the same type of images, a sort of classification. An in-depth study in this sense is desirable to provide new guidelines for the design of fuzzy classification systems.

15 Remark

Literatures are not represented in chronological order.

Compliance with ethical standards

Conflict of interest The authors declare that they have no conflict of interest.

A Proof of Theorem 1

Remark 9 Let us consider three fuzzy images, $F(\mathbf{I}_{norm})_j$, $j = 1, 2, 3$, whose gray levels are $\hat{a_{ij}}$, $\hat{b_{ij}}$, and $\hat{c_{ij}} \in X$, respectively. Let us say, for simplicity, that

$$\begin{aligned} m_{F(\mathbf{I}_{norm})_1}(\hat{a_{ij}}) - m_{F(\mathbf{I}_{norm})_2}(\hat{b_{ij}}) &= \alpha, \\ m_{F(\mathbf{I}_{norm})_2}(\hat{b_{ij}}) - m_{F(\mathbf{I}_{norm})_3}(\hat{c_{ij}}) &= \beta, \\ m_{F(\mathbf{I}_{norm})_3}(\hat{c_{ij}}) - m_{F(\mathbf{I}_{norm})_1}(\hat{a_{ij}}) &= \gamma, \end{aligned} \tag{26}$$

such that $\alpha + \beta + \gamma = 0$. Further, with (26) taken into account, $d(F(\mathbf{I}_{norm})_1, F(\mathbf{I}_{norm})_2)$, $d(F(\mathbf{I}_{norm})_2, F(\mathbf{I}_{norm})_3)$, and

$d(F(\mathbf{I}_{norm})_3, F(\mathbf{I}_{norm})_1)$, as the generic addends of $D(F(\mathbf{I}_{norm})_1, F(\mathbf{I}_{norm})_2)$, $D(F(\mathbf{I}_{norm})_2, F(\mathbf{I}_{norm})_3)$, and $D(F(\mathbf{I}_{norm})_1, F(\mathbf{I}_{norm})_1)$, can be written as follows:

$d(F(\mathbf{I}_{norm})_1, F(\mathbf{I}_{norm})_2) = 2 - (1 - \alpha))\mathrm{e}^{\alpha} - (1 + \alpha)\mathrm{e}^{-\alpha}$, $d(F(\mathbf{I}_{norm})_2, F(\mathbf{I}_{norm})_3) = 2 - (1 - \beta))\mathrm{e}^{\beta} - (1 + \beta))\mathrm{e}^{-\gamma}$, $d(F(\mathbf{I}_{norm})_3, F(\mathbf{I}_{norm})_1) = 2 - (1 - \gamma))\mathrm{e}^{\gamma} - (1 + \gamma))\mathrm{e}^{-\gamma}$. If they have the values

$$d(F(\mathbf{I}_{norm})_1, F(\mathbf{I}_{norm})_2) \geq 0, \tag{27}$$

$$d(F(\mathbf{I}_{norm})_1, F(\mathbf{I}_{norm})_2) = 0 \Leftrightarrow A = B, \tag{28}$$

$$d(F(\mathbf{I}_{norm})_1, F(\mathbf{I}_{norm})_2) = d(F(\mathbf{I}_{norm})_2, F(\mathbf{I}_{norm})_1), \tag{29}$$

$$\begin{aligned} &d(F(\mathbf{I}_{norm})_1, F(\mathbf{I}_{norm})_2) \\ &+ d(F(\mathbf{I}_{norm})_3, F(\mathbf{I}_{norm})_1), \end{aligned} \tag{30}$$

then, with the double summation operator applied to them, (8), (9), (10), and (11) apply.

We prove (27).

If (27) is true, then $d(F(\mathbf{I}_{norm})_1, F(\mathbf{I}_{norm})_2) = 2 - (1 - \alpha)\mathrm{e}^{\alpha} - (1 + \alpha)\mathrm{e}^{-\alpha} \geq 0$, from which $2 \geq (1 - \alpha)\mathrm{e}^{\alpha} + (1 + \alpha)\mathrm{e}^{-\alpha} = \mathrm{e}^{\alpha} - \alpha\mathrm{e}^{\alpha} + \mathrm{e}^{-\alpha}\alpha\mathrm{e}^{-\alpha} = (\mathrm{e}^{\alpha} + \mathrm{e}^{-\alpha}) - \alpha(\mathrm{e}^{\alpha} - \mathrm{e}^{-\alpha})$. Then, $2 \geq 2\cosh(\alpha) - 2\alpha\sinh(\alpha)$ and, again, $1 \geq \cosh(\alpha) - \alpha\sinh(\alpha)$. Now, we set $f(\alpha) = \cosh(\alpha) - (\alpha)\sinh(\alpha)$. However, aiming to search for the minimum value of $f(\alpha)$, we impose $f'(\alpha) = \sinh(\alpha) - \sinh(\alpha) - \alpha\cosh(\alpha) = 0$ to achieve $\alpha\cosh(\alpha) = 0$. $\cosh(\alpha) = 0$ is never null, hence the stationary value of $f(\alpha)$ that one has for $\alpha = 0$. Again, if $\alpha = 0, f(\alpha) = 1$, while, if $\alpha = 1, f(\alpha) = \frac{1}{e} < 1$. From this, α is a point of maximum for $f(\alpha)$. Thus, $1 \geq \cosh(\alpha) - \alpha\sinh(\alpha)$ is always true. Then, given Remark 9, inequality (8) is also verified.

We prove (28).

The sufficient condition is easy to prove. In fact, if $F(\mathbf{I}_{norm})_1 = F(\mathbf{I}_{norm})_2$, then $\alpha = 0$. Thus, $d(F(\mathbf{I}_{norm})_1, F(\mathbf{I}_{norm})_2) = 2 - (1 - \alpha)\mathrm{e}^{\alpha} - (1 + \alpha)\mathrm{e}^{-\alpha} = 0$. Vice versa, to prove the necessary condition, we impose $d(F(\mathbf{I}_{norm})_1, F(\mathbf{I}_{norm})_2) = 0$, obtaining $2 = (1 - \alpha)\mathrm{e}^{\alpha} - (1 + \alpha)\mathrm{e}^{-\alpha} = 0$. Further, it is reasonable to write the following chain of equalities: $2 = (1 - \alpha)\mathrm{e}^{\alpha} + (1 + \alpha)\mathrm{e}^{-\alpha} = \mathrm{e}^{\alpha} - \alpha\mathrm{e}^{\alpha} + \mathrm{e}^{-\alpha} + \alpha\mathrm{e}^{-\alpha} = \mathrm{e}^{\alpha} + \mathrm{e}^{-\alpha} - \alpha(\mathrm{e}^{\alpha} - \mathrm{e}^{-\alpha}) - \alpha(\mathrm{e}^{\alpha} - \mathrm{e}^{-\alpha}) = \mathrm{e}^{\alpha} + \mathrm{e}^{-\alpha} - \alpha(\mathrm{e}^{\alpha} - \mathrm{e}^{-\alpha}) = 2\cosh(\alpha) - 2(\alpha)\sinh(\alpha)$ to achieve $1 = \cosh(\alpha) - \alpha\sinh(\alpha)$ verified *iff* $\alpha = 0$. Thus, (28) is verified. Finally, by Remark 9, (9) is verified.

We prove (29).

$d(F(\mathbf{I}_{norm})_1, F(\mathbf{I}_{norm})_2) = 2 - (1 - \alpha)\mathrm{e}^{\alpha} - (1 + \alpha)\mathrm{e}^{-\alpha} = 2 - (1 - \alpha)\mathrm{e}^{-\alpha} - (1 + \alpha)\mathrm{e}^{-\alpha} = \mathrm{d}(\mathrm{F}(\mathbf{I}_{\mathrm{norm}})_2, F(\mathbf{I}_{norm})_1)$.

We prove (30).

$d(F(\mathbf{I}_{norm})_1, F(\mathbf{I}_{norm})_2) = 2 - (1 - \alpha)\mathrm{e}^{\alpha} - (1 + \alpha)\mathrm{e}^{-\alpha} \leq 2 - (1 - \beta)\mathrm{e}^{\beta} - (1 + \beta)\mathrm{e}^{-\beta} + 2 - (1 - \gamma)\mathrm{e}^{\gamma} - (1 + \gamma)\mathrm{e}^{-\gamma}$, from which

$$\begin{aligned} d(F(\mathbf{I}_{norm})_1, F(\mathbf{I}_{norm})_2) \leq\ & 2 - (1 + \alpha + \gamma)\mathrm{e}^{-\alpha-\gamma} \\ & - (1 - \alpha - \gamma)\mathrm{e}^{\alpha+\gamma} + \times\gamma\mathrm{e}^{\alpha+\gamma} + 2 - (1 - \gamma)\mathrm{e}^{\gamma} \\ & - (1 + \gamma)\mathrm{e}^{-\gamma}. \end{aligned} \tag{31}$$

By (31), we can write $d(F(\mathbf{I}_{norm})_1, F(\mathbf{I}_{norm})_2) \leq 2 - (1 + \alpha)^{-\alpha-\gamma} - \gamma\mathrm{e}^{-\alpha-\gamma} - (1 - \alpha)\mathrm{e}^{\alpha+\gamma} + \gamma\mathrm{e}^{\alpha+\gamma} + 2 - (1 - \gamma)\mathrm{e}^{\gamma} - (1 + \alpha)\mathrm{e}^{-\alpha}$. Further, by adding and subtracting $(1 + \alpha)\mathrm{e}^{-\alpha} + (1 - \alpha)\mathrm{e}^{\alpha}$, we obtain

$$\begin{aligned} d(F(\mathbf{I}_{norm})_1, F(\mathbf{I}_{norm})_2) \leq\ & 2 - (1 + \alpha)\mathrm{e}^{-\alpha} - (1 - \alpha)\mathrm{e}^{\alpha} \\ & + (1 + \alpha)\mathrm{e}^{-\alpha} + (1 - \alpha)\mathrm{e}^{\alpha} - (1 + \alpha)\mathrm{e}^{-\alpha)-\gamma} - \gamma\mathrm{e}^{-\alpha-\gamma} \\ & - (1 - \gamma)\mathrm{e}^{\alpha+\gamma} + \gamma\mathrm{e}^{\alpha+\gamma} + 2 - (1 - \gamma)\mathrm{e}^{\gamma} - (1 + \gamma)\mathrm{e}^{-\gamma}. \end{aligned} \tag{32}$$

In (32), $2 - (1 + \alpha)\mathrm{e}^{-\alpha} - (1 - \alpha)\mathrm{e}^{\alpha} = \mathrm{d}(\mathrm{F}(\mathbf{I}_{\mathrm{norm}})_1, F(\mathbf{I}_{norm})_2)$, while $2 - (1 - \gamma)\mathrm{e}^{\gamma} - (1 + \gamma)\mathrm{e}^{-\gamma} = \mathrm{d}(\mathrm{C}, \mathrm{A})$. Then, (32) becomes

$$\begin{aligned} &d(F(\mathbf{I}_{norm})_1, F(\mathbf{I}_{norm})_2) \\ &+ (1 - \alpha)\mathrm{e}^{\alpha} - (1 + \alpha)\mathrm{e}^{-\alpha-\gamma} - \gamma\mathrm{e}^{-\alpha-\gamma} \\ &- (1 - \alpha)\mathrm{e}^{\alpha+\gamma} + \mathrm{d}(\mathrm{F}(\mathbf{I}_{\mathrm{norm}})_3, \mathrm{F}(\mathbf{I}_{\mathrm{norm}})_1), \end{aligned} \tag{33}$$

thereby reducing the problem to show that $(1 + \alpha)\mathrm{e}^{-\alpha} + (1 - \alpha)\mathrm{e}^{\alpha} - (1 + \alpha)\mathrm{e}^{-\alpha-\gamma} - \gamma\mathrm{e}^{-\alpha-\gamma} - (1 - \alpha)\mathrm{e}^{\alpha+\gamma}$ in (33) is not negative. However, $(1 + \alpha)\mathrm{e}^{-\alpha} \geq 0$ and $(1 - \alpha)\mathrm{e}^{\alpha} \geq 0$.. Thus, it remains to be shown that $-(1 + \alpha)\mathrm{e}^{-\alpha-\gamma} - \gamma)\mathrm{e}^{-\alpha-\gamma} - (1 - \alpha)\mathrm{e}^{\alpha+\gamma} + \gamma\mathrm{e}^{\alpha+\gamma} \geq 0$. If, absurdly, it were $-(1 + \alpha)\mathrm{e}^{-\alpha-\gamma} - \gamma\mathrm{e}^{-\alpha-\gamma} - (1 - \alpha)\mathrm{e}^{\alpha+\gamma} + \gamma\mathrm{e}^{\alpha+\gamma} < 0$, we would get

$$\begin{aligned} \gamma\mathrm{e}^{\alpha+\gamma} &< (1 + \alpha)\mathrm{e}^{-\alpha-\gamma} + \gamma\mathrm{e}^{-\alpha-\gamma} + (1 - \alpha)\mathrm{e}^{\alpha+\gamma} \\ &= (1 + \alpha + \gamma)\mathrm{e}^{-\alpha-\gamma} + (1 - \alpha)\mathrm{e}^{\alpha+\gamma}, \end{aligned} \tag{34}$$

from which $\gamma < (1+\alpha+\gamma)\frac{e^{-\alpha-\gamma}}{e^{\alpha+\gamma}} + (1-\alpha)$. If (34) is always true, it is necessary that $\sup\{\gamma\} < \inf\{(1+\alpha+\gamma)\frac{e^{-\alpha-\gamma}}{e^{\alpha+\gamma}} + (1-\alpha)\}$. However, $\inf\{1 - m_B(b_{ij}) - m_A(a_{ij})\} = 0$ for which $\inf\{1+\alpha+\gamma\} = 0$ and $\sup\{\gamma\} = 1$ which results in a false inequality. Thus, (30) is true and, by Remark 9, (11) holds.

References

1. Gonzales, R.C., Woods, R.F.: Digital Image Processing. Prentice-Hall, New York (2007)
2. Kaur, D., Kayr, Y.: Various image sementation techniques: a review. Int J Comput Sci Mobile Comput **3**(5), 414–809 (2014)
3. Zhang, S., Ma, Z., Zhang, G., Lei, T., Zhang, R.: Semantic image segmantation with deep convolutional neural networks and quick shift. Symm. MDPI **12**(427), 1–1 (2020)
4. Pont-Tuset, J., Arbelaez, P., Barron, J.T., Marquez, F., Malik, J.: Multiscale combinatorial grouping for image segmentation and object proposal generation. IEEE Trans. Pattern Recogn. (2016). https://doi.org/10.1109/TPAMI.2016.2537320
5. Li, H.S., Qingxin, Z., Lan, S., Shen, C.Y., Zhou, R., Mo, J.: Image storagem retrieval, compression and segmentation in a quantum system. Quant. Inf. Process. **12**(6), 2269–2290 (2013)
6. Qasim, A.J., Din, R.E., Alyousuf, F.Q.A.: Review on techniques and file formats of image compression. Bull. Electr. Eng. Inf. **9**(2), 602–610 (2020)
7. Combettes, P.L., Pesquet, J.C.: Proximal Splitting Methods in Signal Processing, Fixed-Point Algorithms for Inverse Problems in Science and Engineering, pp. 185–212 (2011)
8. Peng, B., Zhang, L., Zhang, D.: A Survey of graph theoretical approaches to image segmentation. Pattern Recogn. **46**(3), 1020–1038 (2013)
9. Hay, G.J., Castilla, G., Wulder, M.A., Ruiz, J.R.: An automated object-based approach for the multiscale image segmentation of forest scense. Int. J. Appl. Earth Observ. Geoinform **7**(4), 339–359 (2005)
10. Sharon, E., Brandt, A., Basri, R.: Fast multiscale image segmentation. IEEE Comput. Soc. Conf. Comput. Vis. Pattern Recogn. **1**, 70–77 (2020)
11. Russ, J.C., Brent Neal, F.: The Image Processing Handbook. CRC Press, Boca Raton (2018)
12. Zhang, K., Zhang, Y., Wang, P., Tian, Y., Yang, J.: An improved sobel edge algorithm and FPGA implementation. In: Proceedings of the 8th International Congress of Information and Communication Technology (ICICT-2018), Procedia Computer Science, 131, pp. 243–248 (2018)
13. Meltsov, V., Lapitsky, A.A, Rostovtsev, V.S.: FPGA-Implementation of a prediction module based on a generalized regression neural network. In: Proceedings of the IEEE Conference of Russian Young Researchers in Electrical and Electronic Engineering (EIConRus) (2020)
14. Cao, J., Chen, L., Wang, M., Tian, Y.: Implementating a parallel image edge detection algorithm based on the Otsu–Canny operator on the hadoop platform. Comput. Intell. Neurosci. **3598284**, 1–12 (2018)
15. Verma, O.P., Parihar, A.S.: An optimal fuzzy system for edge detection in color image using bacterial foraging algorithm. IEEE Trans. Fuzzy Syst. **25**(1), 114–127 (2017)
16. Pattanaik, A., Mishra, S., Rana, D.: Comparative study of edge detection using Renyi entropy and differential evolution. Int. J. Eng. Res. Technol. **4**(3), 1001–1005 (2015)
17. Chaira, T., Ray, A.K.: Fuzzy Image Processing and Application with MatLab. Taylor & Francis Group, CRC Press, Boca Raton, London, New York (2010)
18. Chaira, T.: Medical Image Processing, Advanced Fuzzy Set Theoretic Techniques. Taylor & Francis Group, CRC Press, Boca Raton, London, New York (2015)
19. Pradeep Kumar Reddy, R., Nagaraju, C.: Improved canny edge detection technique using S-membership function. Int. J. Eng. Adv. Technol. (IJEAT) **8**(6), 43–49 (2019)
20. Mittal, M., et al.: An efficient edge detection approach to provide better edge connectivity for image analysis. IEEE ACCESS **7**, 33240–33255 (2019)
21. Ma, X., Liu, S., Hu, S., Geng, P., Liu, M., Zhao, J.: SAR image edge detection via sparse representation. Soft Comput. **22**(8), 2507–2515 (2018)
22. Chen, S.C., Cheng Chiu, C.C.: Texture construction edge detection algorithm. Appl. Sci. (MDPI) **9**, 1–25 (2019)
23. Wang, X., et al.: Detection and localization of image forgeries using improved mask regional convolutional neural network. Math. Biosci. Eng. **16**(5), 4581–4593 (2019)
24. Sonka, M., et al.: Image Processsing. Analysis and Machine Vision. Brooks/Cole Publisher, London (2001)
25. Hagara, M., Kubinec, P.: About edge detection in digital images. Radioengineering **27**(4), 1–11 (2018)
26. Sekehravani, E.A., Babulak, E., Masoodi, M.: Implementing Canny edge detection algorithm for noisy image. Bull. Electr. Eng. Inf. **9**(4), 1404–1410 (2020)
27. Nanda, A., et al.: Image edge detection using fractional calculus with features and contrast enhancement. Circ. Syst. Signal Process. **37**, 3946–3972 (2018)
28. Albuquerque, M.P., Esquef, I.A., Gesualdi Mello, A.R.: Image Thresholding using Tsallis entropy. Pattern Recogn. Lett. **25**, 1059–1065 (2004)
29. Sahoo, P.K., Arora, G.: A thresholding method based on two-dimensional Reny's entropy. Pattern Recogn. **37**, 1149–1161 (2004)
30. Kenneth, H., Ohnishi, H.L., Ohnishi, N.: FEDGE-Fuzzy Edge Detection by Fuzzy Categorization and Classification of Edge, Fuzzy Logic in Artificial Intelligence, JCAI'95 Workshop, pp. 182–196 (1995)
31. Silva, L.E.V., SenraFilho, A. C. S., Fazan, V.P.S., Felipe, J.C., MurtaJunior, L.O.: Two-dimensional sample entropy: assessing image texture through irregularity. Biomed. Phys. Eng. Express. (1976). https://doi.org/10.1088/2057-1976/2/4/045002
32. Sadykova, D., James, A.P.: Quality assessment metrics for edge detection and edge-aware filtering: a tutorial review. https://doi.org/10.1109/ICACCI.2017.8126200
33. Panetta, K., Gao, C., Agaian, S., Nercessian, S.: Nonreference medical image edge map measure. Int. J. Biomed. Imaging **2014**, 1–8 (2014)
34. Bausys, R., Karakeviciute-Januskeviciene, G., Cavallaro, F., Usovaite, A.: Algorithm selection for edge detection in satellite images by neutrosophic WASPAS method. Sustain. MDPI **12**, 1–12 (2020)
35. Versaci, M., La Foresta, F., Morabito, F.C., Angiulli, G.: A fuzzy divergence approach for solving electrostatic identification problems for NDT applications. Int. J. Appl. Electromagn. Mech. **1**, 1–14 (2018). https://doi.org/10.3233/JAE-170043
36. Vollmer, M., Mollmann, K.P.: Infrared Thermal Imaging. WILEY-YCH Verlag GmbH & Co, New York (2018)
37. Ieracitano, C., Panto, F., Mammone, N., Paviglianiti, A., Frontera, P., Morabito, F.C.: Towards an Automatic Classification of SEM Images of Nanomaterial via a Deep Learning Approach. Multidisciplinary Approaches to Neural Computing, in press
38. Versaci, M., Calcagno, S., Morabito, F.C: Image contrast enhancement by distances among points in fuzzy hyper-cubes. In:

Lecture Notes in Computer Science, vol. 9257, pp. 494–505 (2015)
39. Versaci, M., Calcagno, S., Morabito, F.C.: Fuzzy geometrical approach based on unit hyper-cubes for image contrast enhancement. In: Proceedings of the IEEE International Conference on Signal and Image Processing (ICSIPA 2015), Kuala Lumpur, Malaysia, pp. 488–493 (2015)
40. Versaci, M., Morabito, F.C., Angiulli, G.: Adaptive image contrast enhancement by computing distances int a 4-dimensional fuzzy unit hypercube. IEEE Access **5**, 26922–26931 (2017). https://doi.org/10.1109/ACCESS.2017.2776349
41. Pavo, J., Gasparics, A., Sebestyen, I., Vertesy, G., Darczi, C.S., Miya, K.: Eddy Current Testing with Fluxset Probe. Applied Electromagnetics and Mechanics. JSAEM, Tokyo (1996)
42. Doshi, J., Reneker, D.H.: Electrospinning process and applications of electrospunfibers. J. Electrostat. **35**(2–3), 151–160 (1995)
43. Vilchez, A., Acevedo, F., Cea, M., Seeger, M., Navia, R.: Applications of electrospun nanofibers with antioxidant properties: a review. Nanomater. MDPI **10**(175), 1–25 (2020)
44. Fenn, J.B., Mann, M., Meng, C.K., Wong, S.D.F., Whitehouse, C.M.: Electrospray ionization for mass spectrometry of large biomolecules. Science **246**(4926), 64–71 (1989)
45. Versaci, M., Morabito, F.C.: Fuzzy time series approach for disruption prediction in tokamak reactors. IEEE Trans. Magn. **39**(3), 1503–1506 (2003)

Mario Versaci received his degree in civil engineering from the "Mediterranea" University, Italy, where he also he received a PhD in electronic engineering. He also received the Diplome d'Etudes Approfondites at the Grenoble Electrotechnics Lab. In the "Mediterranea" university, he serves as both Associate Professor of electrical engineering and scientific head of the NDT/NDE Lab. He received a degree in mathematics from the University of Messina. His research focuses on soft computing, image processing, and MEMS/NEMS.

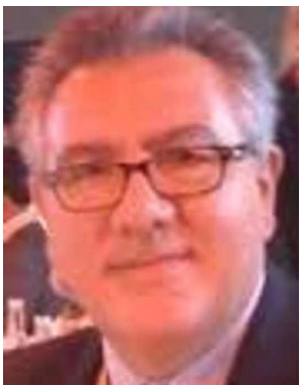

Francesco Carlo Morabito is a Full Professor of Electrical Engineering at the "Mediterranea" University of Reggio Calabria, Italy. Former Dean of the Faculty of Engineering, he is now serving as Vice-Rector for International and Institutional Relations. Governor of the International Neural Network Society for 12 years, he served as President of the Italian Network Society (2008–2014). He is a Foreign Member of the Royal Academy of Doctors, Spain, and a member of the editorial boards of international journals, including the International Journal of Neural Systems, Neural Networks, and Renewable Energy. He is author or coauthor of more than 350 papers in international journals/conference proceedings in various fields of engineering (radar data processing, nuclear fusion, biomedical signal processing, nondestructive testing evaluation, and computational intelligence). He is co-author of 10 books and held 3 international patents.